EXPERIMENTAL AND NUMERICAL CHARACTERIZATION OF HARBOR OSCILLATIONS IN THE PORT OF MÁLAGA, SPAIN

S. Sammartino[1], J.C. Sánchez Garrido, J. Delgado, C. Naranjo,

F. Criado Aldeanueva, J. García Lafuente,

Physical Oceanography Group, University of Málaga, Campus de Teatinos s/n, 29071, Málaga, Spain

ABSTRACT

The port of Malaga is routinely affected by short period sea level oscillations whose amplitudes, typically of few cm, can sporadically outweigh the tidal variations. High frequency oscillations in the innermost basins may cause problems of stability of the moored crafts. This has motivated the characterization of the resonant behavior of the port and its response to external forcing carried out by experimental and numerical approaches. The Helmholtz mode of the harbor has been found at ~16.5 minutes period, in both the observed data and the numerical experiments. A second mode, of period around 6-7 minutes, beyond the temporal resolution of the tide gauge, has been detected only in the numerical results. The typical scenario during the episodes of harbor oscillations is low pressure (75% of the cases) accompanied by bursts of high frequency disturbance of the pressure field, usually occurring during the transit of atmospheric fronts over the Iberian Peninsula. Winds appear to be of secondary influence although the oscillations seem to occur principally under westerlies.

[1] Corresponding author: Simone Sammartino

Tel.: +34 952 13 28 49

E-mail address: ssammartino@ctima.uma.es

Although results are not conclusive, some resonance mechanisms (Proudman and Greenspan resonance) for transferring energy from the atmosphere to the ocean have been considered as the last process to generate the harbor oscillations.

Keywords: Harbor resonance; Sea level oscillations; Resonance modes; MITgcm.

1. Introduction

The Port of Málaga is located in the middle of the Málaga Bay, facing to the Alboran Sea, at the southwestern margin of the Mediterranean Sea (Figure 1). It has a relevant role in the commercial economy of the Spanish region of Andalusia, competing with the bigger infrastructures of the ports of Algeciras (Strait of Gibraltar) and Tanger-Med (Tangier, Morocco), but it is mostly devoted to touristic activities as shipping cruise and watercraft facilities. The Port has summed around 1 million passengers in 2011 (http://www.malagaport.net/publicaciones.html) both from international cruises, regular shipping lines and private nautical tourism.

Since 1997 the port has undergone a series of massive structural reforms such as the building of the eastern breakwater in 1997 and the container terminal in 1999 (Figure 1b), which has noticeably increased its overall length and improved its commercial capabilities. Currently the local Port Authority is working out a plan to enhance the receptivity of small and medium ships, yachts and boats by installing new docks and facilities in the inner basins of the port. However they have to face problems of stability of the moored crafts due to high frequency and small amplitude sea level oscillations that might well raise undesirable nuisance to potential users and, therefore, put the foreseen plan in question.

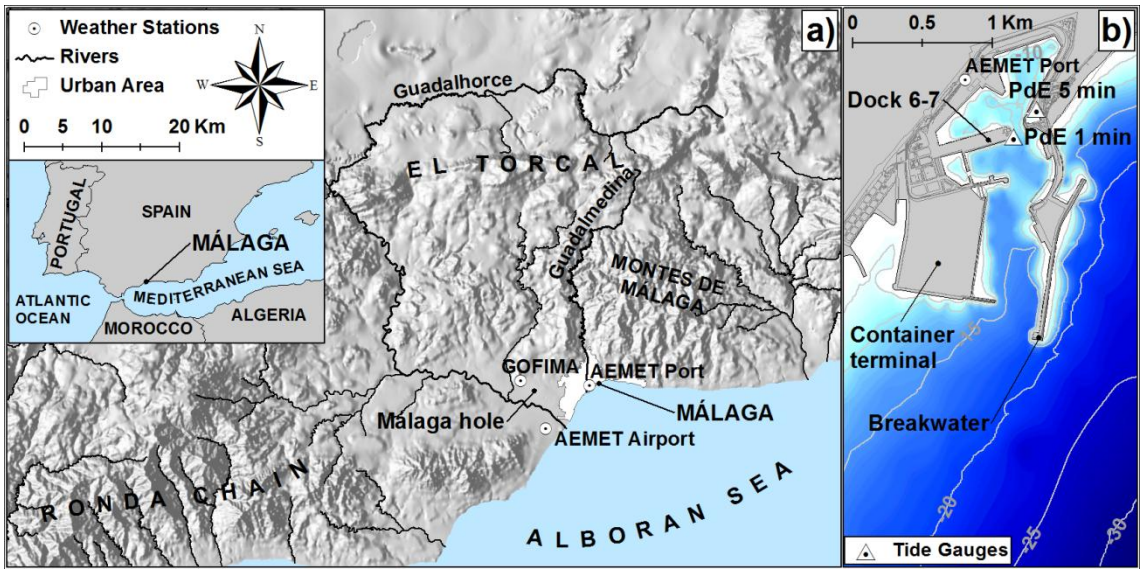

Figure 1 - Panel a): map of the Province of Málaga. Weather stations are represented in white circles. The main rivers and geographical structures cited in the work are indicated. Panel b): map of the Port of Málaga. The two tide gauges analyzed are represented in white triangle.

To a lesser extent, the observed situation in the port of Málaga recalls the well-known phenomenon of the 'rissaga' in Menorca Island in the Spanish Balearic Archipelago (Monserrat, et al., 1991; Monserrat, et al., 1992; Gomis, et al., 1993; Garcies, et al., 1996; Monserrat, et al., 2006), the 'marrobbio' in Sicily (Candela, et al., 1999) or the 'abiki' in Japan (Hibiya, et al., 1982), where particular conditions of multiple resonances and a hazardous coupling between atmosphere and ocean induce catastrophic sea level oscillations (surges) causing associated damages for millions of dollars. Rabinovich (2009) describes this kind of phenomena as 'harbor oscillations', differentiating it from the well-known 'seiches'. The latter are water level oscillations of closed basins, typically lakes, induced by the direct action of external meteorological or seismic forcing. The input disturbances trigger a series of oscillations of the surface with different frequencies, which depend on the geometry of the basin, and amplitude, which depends on the energy transfer from the external force. This energy transfer in turn is a function of the strength of the external force and, more importantly, the prevailing

frequency, which may eventually lead to resonance. Friction and gravity gradually restore the equilibrium.

The harbor oscillations, or coastal seiches (Drago, 2008), concern semi-enclosed basins (harbors, inlets or bays) and are generated by the arrival of long waves coming from the open sea. More complex (multiple) resonances may occur during the energy transfer from the atmosphere to the sea surface and from the open sea to the harbor, while the main mechanism of dissipating this energy is by radiation through the open boundary (Rabinovich, 2009). A relevant issue in harbor oscillations is the associated currents (harbor currents) that can generate further resonance and possibly damages to the moored ships (Sawaragi, et al., 1982).

The present work aims at investigating the dynamic response of the port of Málaga to external forcing and the possible generation of coastal seiches and high frequency sea level oscillations. The paper is organized as follows: Section 2 presents the experimental datasets. The harbor oscillations are characterized in Section 3 from the observation, while a theoretical and numerical treatment of the harbor dynamics is provided in Sections 4 and 5. Section 6 investigates the atmospheric forcing for the occurrence of the events and, finally, Section 7 presents the conclusions. Appendix A details the run of the numerical experimental discussed in the work.

2. Available datasets

Sea level

Sea level data were provided by the Spanish State Port Authority (Puertos del Estado, PdE hereinafter), which has had two different tide gauges installed inside the port of Málaga. The oldest one, based on ultrasonic technology, was placed on the inner dock of a small marina

along the eastern edge of the harbor and was working from July 1992 to April 2010 storing data every 5 minutes (*PdE 5 min* in Figure 1b). In January 2009, a new tide gauge, based on radar technology, was installed on the external corner of dock 6-7 at the opposite side of the harbor (*PdE 1 min* in Figure 1b), and is storing data at 1 minute sampling rate. Both of them are part of the REDMAR sea level network of PdE (http://calipso.puertos.es/BD/informes/INT_REDMAR.pdf).

The two series together span over more than 20 years, with a small percentage of missing data (4.5% and 2.3% for the 1 minute and the 5 minutes series, respectively) and overlap from the end of January 2009 to the end of April 2010.

Meteorological variables

Atmospheric pressure and wind direction and speed observations have been daily collected with a six hours sampling rate interval (at 0:00, 07:00, 13:00 and 18:00) from the Málaga Airport and Málaga Port meteorological stations of the Spanish Meteorological Agency (AEMET). Airport station time series span from January 1992 to October 2013 while the Port station series presents different time extent for atmospheric pressure variable (January 2006 to December 2009) and wind (January 2001 to October 2013). Time series with higher sampling rate (15 minutes) collected at a third station located at the Málaga University premises (included in the Meteoclimatic Spanish network of meteorological stations - www.meteoclimatic.es), spanning the period November 2010 to November 2013, have also been used for comparison and check purposes (GOFIMA series). Pressure and wind speed are given in hPa and kmh^{-1}, with a resolution of 0.1 hPa and 1 kmh^{-1}, respectively. Wind speed and direction have been converted in zonal and meridional velocity components.

To have a general vision of the large-scale wind field free of topographic influences, daily gridded sea surface wind ASCAT (Advanced SCATterometer) observations with spatial resolution of 0.25 degree have been downloaded by http://cersat.ifremer.fr/ (Bentamy, et al., 2012). Three cells around the city of Málaga have been averaged to obtain a single wind velocity series of years 2008 and 2009 with daily values.

Figure 2 shows the wind roses of the different datasets. The regional wind regimen is clearly bidirectional, with slight prevalence of westerlies (Figure 2a). Large-scale winds are conveyed by the local topography, which features marked river valleys oriented NW-SE, specially the Guadalhorce river (Figure 1). The first and third quadrants are shielded by "El Torcal" formation and the Ronda chain (Muñoz, 1998), closing the so called "Málaga hole" (a flat depression around the urban nucleus and the valley of the Guadalhorce river) at northeast and at east-southeast, respectively (Figure 1a). The result is the well-known bi-directionality of winds observed in Málaga area (Figures 2b,c), with an overall slight predominance of WNW-NW winds, typical of autumn-winter, over SSE-SE winds, typical of spring-summer.

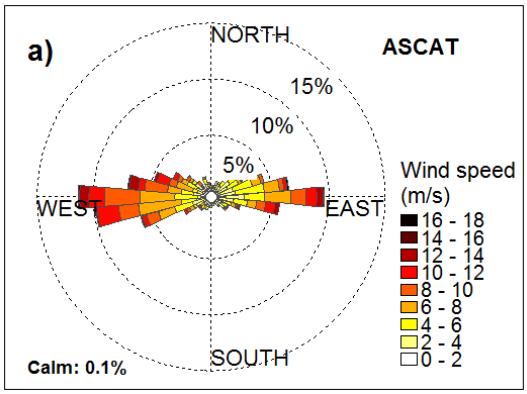

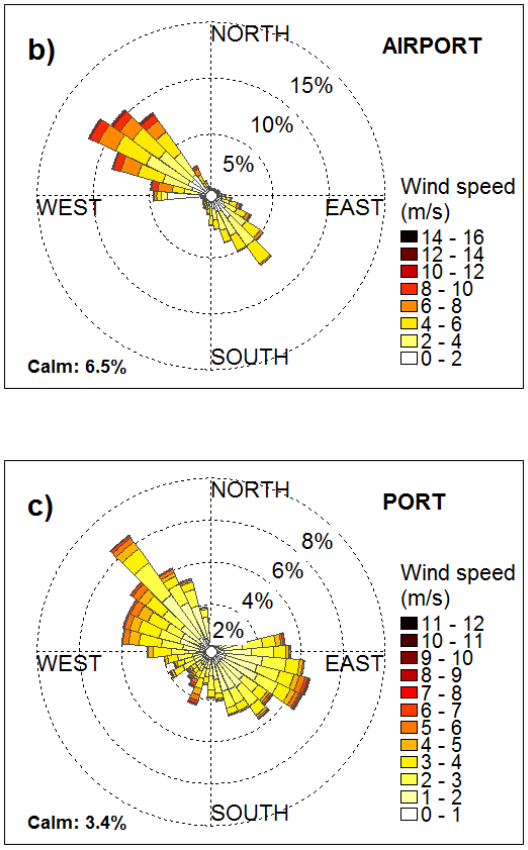

Figure 2 - Wind roses of ASCAT data (panel a), and the Airport (b) and Port (c) weather stations.

3. Short period harbor oscillations

The high frequency oscillations observed inside the Málaga harbor are of few cm amplitude and some tens of minute period. They must be compared with the tidal oscillations, which have amplitudes of 19.2 and 7.3 cm for M2 and S2 constituents, respectively. Therefore semidiurnal amplitudes are typically 12 cm in neap tides, and 26 cm during spring tides. As a rule, the high frequency oscillations are much weaker although they can reach and exceed tidal fluctuations under certain circumstances if they are suitably excited by external forces.

Figure 3 shows the power spectra of the two sea level series available during their common period (20 of January 2009 to 23 of April 2010). The 1 min series (PdE1 hereinafter) shows slightly higher amplitude than the 5 min series (PdE5), especially at the high-frequency end of the spectrum, the difference likely stemming from the different location of the instruments. The PdE1 tide gauge is in the main channel of the harbor, while the PdE5 gauge is sheltered in a small and shallower semi-enclosed basin with a narrow entrance (Figure 1).

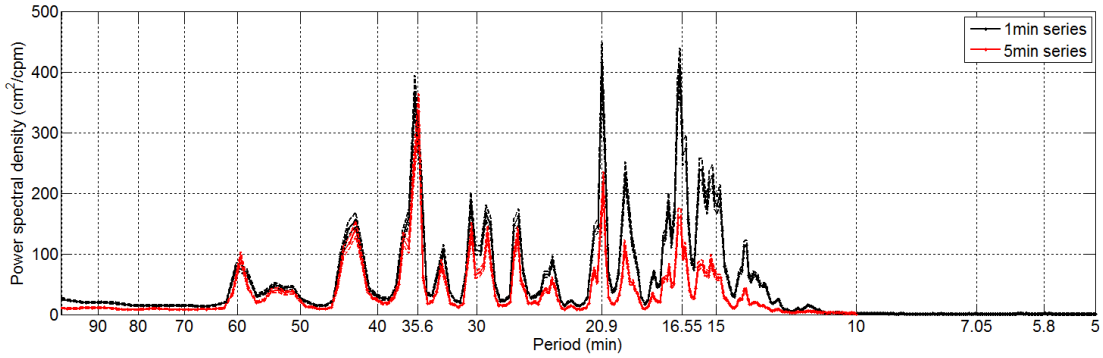

Figure 3 - Power spectra of the PdE1 series (black line) and the PdE5 series (red line). Dashed lines indicate 95% confidence limits.

The analysis of short period oscillations has been carried out on the largest PdE5 series. A number of 17 complete years (from 1 of January 1993 to 31 of December 2009) has been selected in order to avoid seasonal biases in the statistical analysis. The data gaps have been filled in following two different approaches: 1) a linear interpolation whenever the gap was shorter than 6 samples (half an hour) and 2) a reconstruction of the tidal oscillations using the harmonic constants calculated by harmonic analysis (Pawlowicz, et al., 2002) applied to the whole series, in case of gaps larger than 6 samples.

Harbor oscillations are location dependent and its main features are related to the interaction of local dynamics with the harbor structure. However, they are universally recognized to be characterized by an enhancement of energy at the highest frequencies (Rabinovich, 2009). The

spectrum in Figure 3 reveals three more energetic bands around 16.5, 20.9 and 35.6 minutes. In order to properly discriminate their energy content, a series of FIR equiripple band-pass filters (Parks–McClellan algorithm, Oppenheim et al., 1989) have been applied to the series. This kind of filter assures a very weak distortion of the signal around the pass and stop frequencies.

The analysis mainly focuses on the band centered at 16.5 min period. The harbor oscillations are characterized on the basis of a standard deviation-threshold method. A moving window of one hour width has been applied to estimate the variance within every one-hour fragment along the whole PdE5 series and the short period oscillation events have been defined as those having a variance exceeding twice the standard deviation of the whole series (2σ). The number of fragments exceeding such threshold represents around the 3% of the overall series and the number of 'day with at least one event' (DOE hereinafter) sum up the 18.6% of the whole period. They exhibit little seasonality and high interannual variability, as shown in Figure 4b. The average amplitude is quite constant, around 2 cm, while the maximum observed amplitude may be as high as six times the average amplitude and exhibits marked interannual variability as well as a moderate seasonal cycle (Figure 4a).

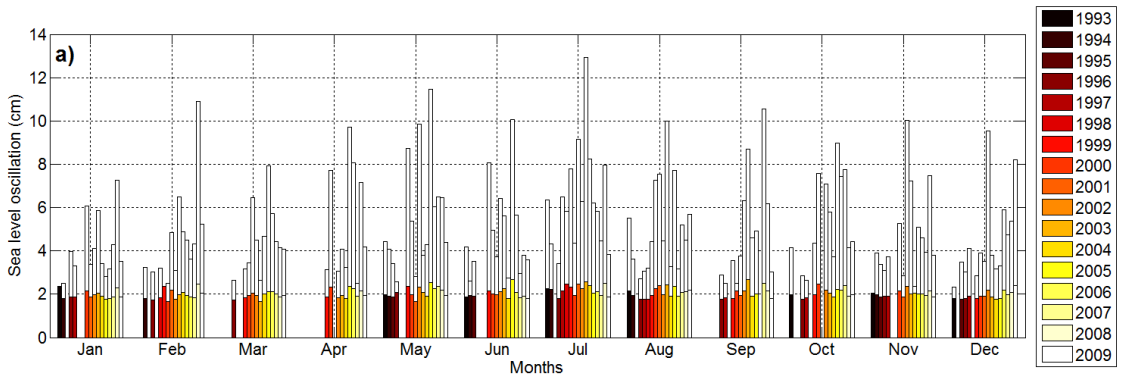

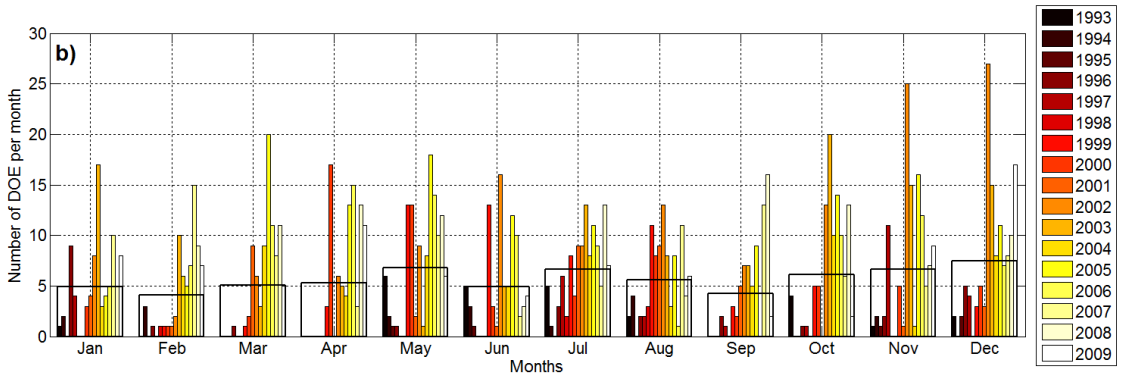

Figure 4 - Panel a): monthly average (color filled bars) and maxima (white bars) amplitude of short period oscillations. Panel b): number of events per month (color filled bars) and its interannual averages (thick empty bar).

The mean amplitude (color filled bars in Figure 4a) seems to be rather constant throughout the year, with a slight higher regimen in the summer months (the highest mean amplitudes are in July). Peaks amplitude (white filled bars in Figure 4a) follow the same pattern, with the highest concentration of maxima in this month and a certain tendency to an annual cycle (higher amplitudes in summer and lower in winter). Superimposed to this seasonal variability, the interannual variability is much more evident: during the first five years of the series (the first five darkest color tones), the amplitudes are highly variable, alternating months of relative strong oscillations, as in January 1993 or July 1993/1994, with others with no events at all, as in March or April 1993-1998. In the year 1999 things seems to change radically, with a quite stable regimen throughout the rest of the series. Maxima indicates some kind of dome-shaped pattern, especially in the spring-summer months, with the highest peaks concentrated in the years 2002-2004, while the winter months show a concentration of higher peaks in the last years of the series.

This situation is generally but not always confirmed by the distribution of the DOE (Figure 4b). The events are globally more abundant in the spring-summer months (May and July) and at

the end of the year (note that in December 2002 the number of events is nearly one per day), confirming the peak amplitude pattern. On the other hand, the highest maxima of July do not coincide with a higher density of events, which are more abundant in the last months of the series, especially in years 2002/2003. For instance, the month of July 2004 presents one of the strongest averaged oscillations of the series and the highest peak at all, while it is relatively poor in abundance of events with respect to the rest of the years (especially after 1999), representing an example of relatively not abundant but highly energetic series of events. On the other hand, the month of October 2003 shows one of the highest abundance of events, while it is not especially high in amplitude. Note that the standard deviation-threshold approach has been submitted to a sensitive test (successfully passed), by iteratively varying the value of the own threshold, in order to validate the choice of the 2σ range. The DOE and amplitude pattern was maintained throughout the test.

A very clear result is the notable increase of both amplitude and rate of occurrence of the events after 1999. Figure 5 shows the total number of DOE throughout the 17 years analyzed for the three frequency bands highlighted in the spectrum of Figure 3.

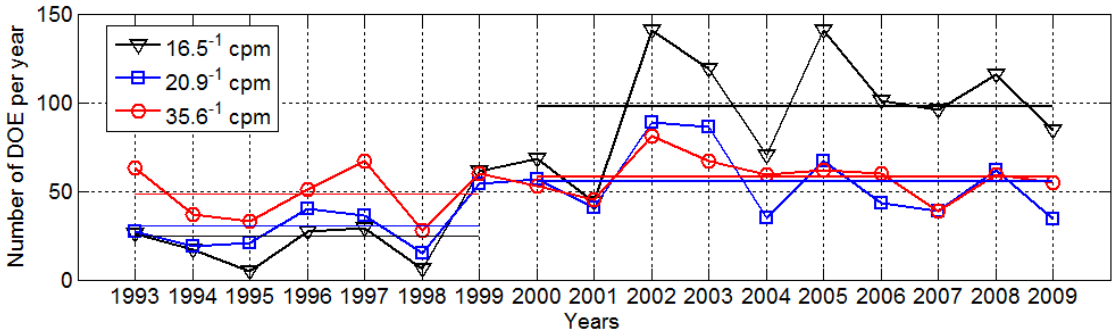

Figure 5 - Number of DOE per year for the three frequency bands discussed in the text. Thin lines are the averages of the periods 1993-1999 and 2000-2009.

The most evident aspect is the marked increase of the number of occurrence of DOE per year from the year 1999 in the higher frequency band series of 16.5^{-1} cpm. It passes from 6 events per year in 1998 to 60 in 1999, further increasing in the following years and stabilizing around 100 events per years from 2002 onward. The average number of DOE quadruples from period 1993-1999 to period 2000-2009 in that frequency band. This issue will be discussed in the next sections.

4. Normal modes

Although the dominant frequencies of the harbor oscillations and their temporal variability have been characterized, their nature has not been clarified. The spectrum in Figure 3 exhibits three marked energy peaks at relatively isolated frequencies that are candidate to be related with resonant oscillations of the system. This is investigated in this section.

Resonant oscillations are standing waves supported by the harbor and, in the absence of friction and rotation, are given by the eigenvalue problem (Wilson, 1972; Delgado, et al., 2011):

$$\frac{\partial}{\partial_x}\left(H\frac{\partial \eta_j}{\partial_x}\right)+\frac{\partial}{\partial_y}\left(H\frac{\partial \eta_j}{\partial_y}\right)+\left(\frac{\omega_j^2}{g}\right)\eta_j=0,\quad j=0,1,2,\ldots \qquad \textbf{(1)}$$

Here H is the bottom depth, g the gravity acceleration, and x, y denote the horizontal spatial coordinates. The eigenvalue is the wave angular frequency ω_j, and the eigenfuction or spatial j-th mode $\eta_j(x,y)$, denoting the free surface vertical displacement. As boundary conditions, a zero flux across the solid boundaries of the harbor and the commonly assumed presence of a nodal line along its mouth have been prescribed. In terms of η these conditions read

$$\frac{\partial \eta_j}{\partial n} = 0, \quad \eta_j = 0 \qquad \textbf{(2)}$$

respectively, with n the spatial component normal to the domain walls.

Following Rueda and Schladow (2002), equations (1) and (2) have been solved by the Galerkin finite element method on the unstructured grid shown in Figure 6a. Figure 6b depicts the Helmholtz mode. It represents the simplest instance of resonant response (quarter-wave resonator) and describes an oscillation with a single nodal line at the harbor mouth and maximal amplitudes at its head (the antinode). Its period is the largest one among all the supported standing waves and in this case is T_0 = 16.5 minutes, which fits fairly well the shorter period at which the observed spectrum presents a maximum. Any oscillation of greater period detected in the harbor, in particular those corresponding to the two energy peaks observed at periods of 20.9 min and 35.6 min, are expected to correspond to external signals rather than to resonant oscillations of the harbor.

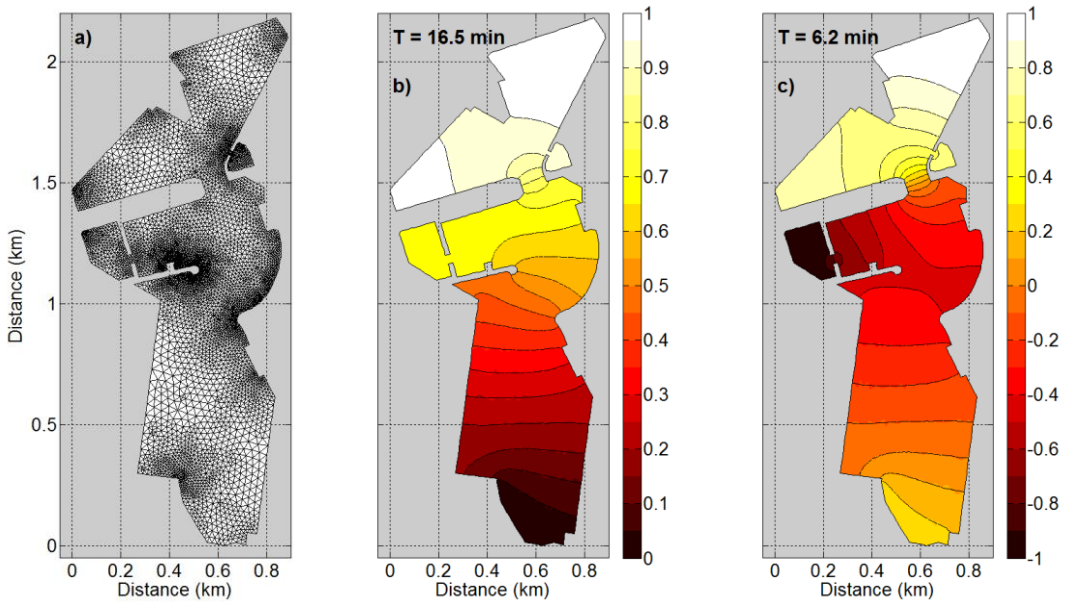

Figure 6 - Panel a): finite element discretization grid used to solve the eigenvalue problem. Panel b) and c): amplitudes of the first and the second modes, respectively. Amplitude is expressed in normalized units.

The n=1 mode (Figure 6c) presents an additional nodal line at the narrower passage of the port, where the PdE1 tide gauge is located, and its period is T_1 = 6.2 minutes. Any oscillation around this period should hence be hardly detected around this location, which is consistent with the PdE1 spectrum where there is no significant energy at that frequency band. On the other hand, amplitudes around the location of PdE5 tide gauge is not null, and therefore should be noted in the corresponding spectrum. Unfortunately this could not be confirmed in our data because T_1^{-1} is higher than the Nyquist frequency of that tide gauge.

5. Resonance curve

Normal modes give natural frequencies and spatial patterns of the expected oscillations in the basin, but do not provide information concerning the sensitivity of its response to external forcing. Additionally, the calculation described before assumes the presence of a nodal line at the harbor mouth. While this is a reasonable approximation, the actual nodal line is usually

observed to lie some distance outside the entrance, and thereby modifies to some extend the calculated resonant frequencies. Numerical models are useful in these regards.

A series of numerical experiments have been conducted in order to (1) study the sensitivity of the harbor response to the characteristics of incident long waves coming from the open sea, and (2) further elaborate the already estimated structure and natural frequencies of the harbor normal modes by a different approach. The model is based on a barotropic configuration of the MITgcm source code (Marshall et al.1997a,b), and its domain covers an area of 6x6 km with the harbor in its northern part. For a given frequency f_r, the model is laterally forced by a periodic velocity field such that it produces an overall sea surface oscillation of 1.5 cm amplitude (see details on model configuration and set up in Appendix A). This mimics the effect of remote atmospheric pressure perturbations of 1.5 hPa acting at frequency f_r.

First consider a run with forcing frequency f_r = 30^{-1} min^{-1}. Figure 7a shows the spectrum of a SSH time series extracted from the head of the harbor, and reveals energy content not only at f_r, but also the presence of a local maxima at f_0 = 16.55^{-1} min^{-1} and a less pronounced peak at f_1 = 7.05^{-1} min^{-1}. This behavior is observed when forcing the model with any other frequency, as illustrated in Figure 7b, which corresponds to a run with f_r = 10^{-1} min^{-1}. Again, there is an energy maximum at the forcing frequency and also at f_0 and f_1, with the latter now being more apparent than in the previous case.

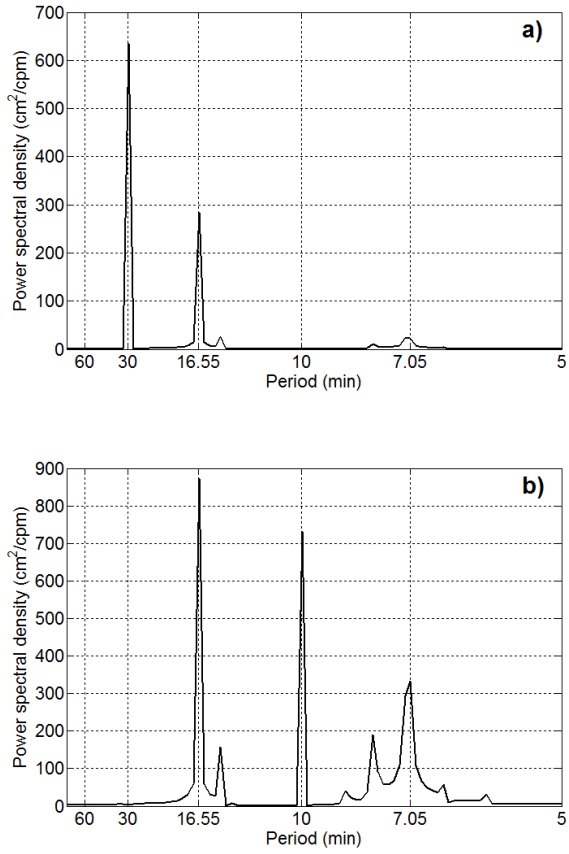

Figure 7 - Power spectra of the simulated sea level time series at one particular location of the head of the harbor. Panels a) and b) correspond to runs with forcing frequency f_r= 30^{-1} min^{-1} and f_r= 10^{-1} min^{-1}, respectively.

This undoubtedly indicates a resonant behavior around f_0 and f_1, and the agreement of these values with the calculated frequencies in Section 4 makes it clear that f_0 and f_1 correspond to the n = 0 and n = 1 resonant modes, respectively. The spatial structure of SSH amplitudes associated to these frequencies confirms this fact (see Figure A1).

The mean amplification factor obtained for all the experiments is shown in Figure 8 (asterisk marks), as a function of all tested forcing frequencies. The maximum is reached at the Helmholtz frequency f_0 = 16.55^{-1} min^{-1} with a factor of ∼18, and decays relatively fast as one

moves away from f_0. This behavior resembles that of a driven harmonic oscillator with small dissipation, and our results actually fit its theoretical amplification factor curve (solid line in Figure 8)

$$Af(f) = \left\{\left[1 - \left(\frac{f_r}{f_0}\right)^2\right]^2 + Q_f^{-2}\left(\frac{f_r}{f_0}\right)^2\right\}^{-1/2} \quad \textbf{(3)}$$

where Q_f = 18 in this case, the so-called quality factor (Q-factor). The only worth noting discrepancy concerns the slight overestimation of Af for f_r = 10^{-1} and f_r = 15^{-1} min^{-1} with respect to the curve, which is attributable to the proximity of these frequencies to the second resonant frequency f_1.

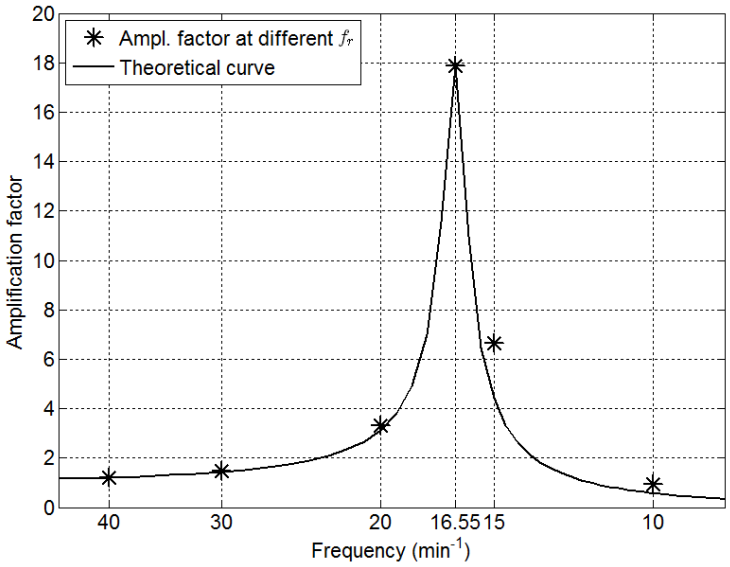

Figure 8 - Mean amplitude amplification factor for f_r = 40^{-1}, 30^{-1}, 20^{-1}, 16.55^{-1}, 15^{-1}, and 10^{-1} cpm (asterisk marks). Solid line is the curved given by equation (3) for f_0 = 16.55^{-1} cpm.

Comparatively to other similar settings we can state that the Málaga harbor has an elevated Q-factor. For instance, the Ciutadella Inlet, in the Balearic Islands, where strong "rissaga" events may occur, has an estimated Q-factor of ~10 for the fundamental mode (Rabinovich, et al.,

1999; Monserrat, et al., 1991), while the Malokurilsk Bay in the Shikotan Island (Japan), exhibits a Q-factor of ~13 (Djumagaliev, et al., 1994). The comparison has to be taken with caution, however, since in these cases the estimates were based on spectral methods applicable to monochromatic series rather than idealized numerical experiments (Rabinovich, 2009). Moreover, at least in the case of the Shikotan Islands, the observations were located at the entrance of the bay while our estimation is based on the averaged amplitude of the whole port domain.

6. Atmospheric forcing

The meteorological conditions for the occurrence of the short period oscillations characterized so far are quite uneven and locally dependent, but a rather clear pattern is visible. Figure 9 shows the monthly distribution of the pressure anomaly during the event. Here the pressure measured in the GOFIMA station has been low-pass filtered, its mean (1016 hPa) has been removed and the averaged anomalies of the six hours before the event has been calculated.

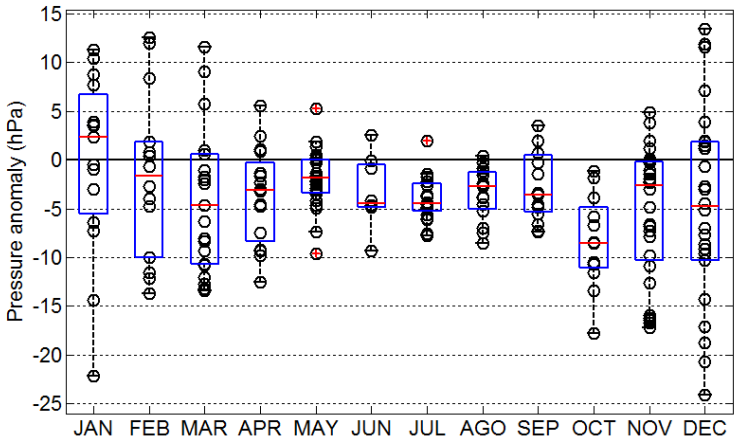

Figure 9 - Box-whiskers plot of pressure anomaly measured in GOFIMA station (see text for computation details) during the events. Median and inter quartile range are represented in red line and blue box, respectively. The whiskers extend to ±1.5 times the inter quartile range, while the outliers (red crosses) are computed as the values

exceeding these limits. Superimposed to the box-whiskers plot are the single values (black circles) of the pressure anomaly.

The general trend is that the events coincide with low pressures (see the median values in Figure 9 always below zero except in January) related with the transit of atmospheric systems (Monserrat, et al., 1992; Monserrat, et al., 2006). Low-pass filtered pressure anomaly and sea level variance are negatively correlated. Their maximum cross-correlation is -0.68 with pressure leading the sea level oscillations by ~3.5 hours. That trend is not a strict rule, however. Pressure in spring/summer months is notably more stable and the events occur almost always in low pressures, whereas the highest variability typical of the autumn/winter period induces an increase of the number of DOE under relatively higher pressure.

Figure 10 shows a typical example of harbor oscillations found in the PdE1 series band-pass filtered at 16.5^{-1} cpm, with sea level oscillations clearly exceeding 10 cm around their mean.

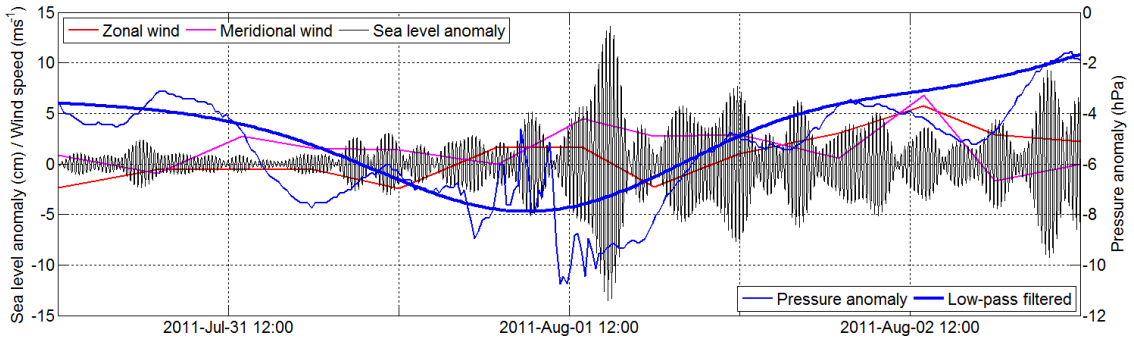

Figure 10 - A fragment of the PdE1 series band-pass filtered at 16.5^{-1} cpm, with overlapped the two wind components measured in the PORT station and the pressure and its low-pass filtered series, measured in GOFIMA station.

The oscillations occur under a low atmospheric pressure situation (pressure anomalies are always negative) and are propitiated by a further drop of atmospheric pressure (with a rate of

about 0.5 hPa per hour), but the main forcing seems to be the high frequency disturbance of the barometric field. In particular the huge atmospheric pressure drop, exceeding 15 hPa in less than one hour, triggers definitely the train of short period oscillations visible in the figure.

Figure 11 shows another fragment of the PdE1 band-pass filtered (at 16.5^{-1} cpm) series representing the most energetic event detected. Sea level oscillations reach 20 cm (peak amplitude) around the mean, with a main wave train followed by a repetition of oscillations that weaken in the subsequent 8 hours approximately. A net peak in the variance of atmospheric pressure occurs approximately 3 hours before, with weaker oscillations following. The inset in the right upper corner of the figure, showing the original series of sea level and pressure, reveals a steep drop of 2.5 hPa in 45 minutes, followed by a series of high frequency oscillations of 0.4 hPa (peak) amplitude lasting for the whole sea level oscillations lifetime. It is especially worth noting that the sea level oscillations occurring during this low tide semi-cycle (spring tide in this case) amply outweigh the tidal sea surface variations.

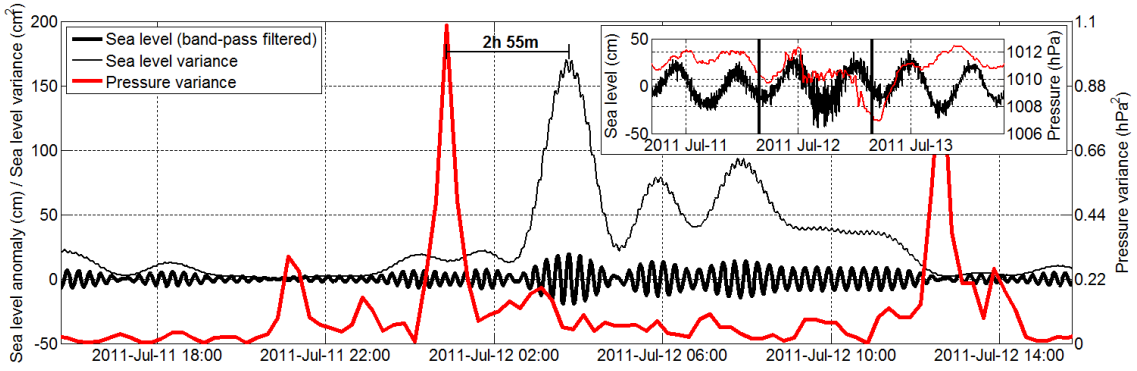

Figure 11 - Band-pass filtered (at 16.5^{-1} cpm) sea level (thick black line), its corresponding variance (thin black line) and pressure variance (thick red line) by the GOFIMA series for the most energetic event found in the PdE1 series. Inset: unfiltered sea level (black) and pressure (red) for a slight larger period. Here the vertical thick bars indicate the temporal limits of the fragment displayed in the main graph.

In order to statistically evaluate the correlation between pressure and sea level oscillations (mostly regarding their respective high frequency variations) a peak-to-peak lag-based approach applied to the variance of both variables has been employed. For each peak of sea level variance a peak of pressure variance (defined using the same 2σ threshold approach used with sea level variance) is sought within 12 hours before the event and, in case it is detected, the temporal lag between the two peaks is computed. Here the peaks of pressure variance are always evidences of the occurrence of a single pressure drop, followed by bursts of high frequency oscillations, or at least of only this last phenomenon. More than 70% of times, a peak of pressure variance has been found and, most of times, it has been detected around 4 hours before the event.

While pressure data recorded in GOFIMA station have proven to be useful to study the high frequency behavior of the barometric field, winds sampled in this station are characterized by a quite poor spatial (angular) resolution (22.5º) and are likely affected by some kind of screening by the surrounding infrastructures. On the other hand, winds sampled in the two AEMET stations show a very low temporal resolution, mostly inadequate to study such a highly variable field. These conditions make the analysis of the wind regimen a quite hard task. At large scale, westerlies prevail over the easterlies (65% versus 35% of cases in the ASCAT dataset), although their distribution is locally distorted by topography. Westerlies are generally turned into NW, although in few cases of strong harbor oscillations (around 5% of the total events) they veer into SW along the coast at west of the city (see for instance the event in Figure 10). However a large number of events (around 33% of cases) also occur under easterlies episodes.

7. Discussion and conclusions

The port of Málaga is routinely affected by short period oscillations whose amplitudes are of few cm as a rule, although they may eventually exceed 20 cm as illustrated in Figure 11. Considering that the amplitude of M2 constituent is ~19 cm, the short period oscillations are comparable or even may outweigh the tide during these extreme events when, therefore, they become relevant.

The spectra in Figure 3 show three prevailing periods for these oscillations that outstand over a rather noisy background. The narrowness of the peaks is suggestive of harbor oscillations (Rabinovich, 2009), a reason that has motivated the analysis of the normal modes of the port. This has been carried out numerically using two different approaches, namely, by solving the eigenvalue problem given by equations (1) and (2), and, secondly, by analyzing the response inside the port produced by a barotropic model driven by external periodic forces (Appendix A).

Both independent approaches provide almost identical results for the spatial structure of the fundamental or Helmholtz mode (compare Figure 6b and A1b) and the same fundamental frequency f_0 = 16.5^{-1} cpm. It corresponds to the peak with the highest frequency of the three highlighted in Figure 3, which indeed confirms that this is the frequency of the fundamental mode of the port. It is worth noting that the barotropic model predicts an amplification factor of 18 at this frequency (Figure 8), which agrees well with the quality factor $Q = f_0/\Delta f$ deduced from the spectrum of Figure 3 using the half-power bandwidth criterion (Emery, et al., 2001) and a Δf of 0.8 - 0.9 min^{-1} from the figure. The coincidence provides new robust arguments for the good performance of the model.

Similar conclusions are drawn for the second mode (Figure 6c and A1c), although the frequencies differ slightly in this case (6.2^{-1} cpm against 7.05^{-1} cpm). Despite its existence, the footprint of this mode is not visible in the spectra of Figure 3 because the only tide gauge able to detect it (PdE1 with its 1 minute sample interval) is placed at the narrowest part of the port

(Figure 1), where the mode has its nodal line. Neither approach indicate the existence of resonant modes with frequencies matching the 20.9^{-1} and 30.5^{-1} cpm peaks of Figure 3, which suggests a different origin for them. This hypothesis is also supported by the fact that the structural reforms of the port completed in year 1999 increased the DOE per year dramatically for the 16.5^{-1} cpm oscillations (which were virtually absent prior to this year, see Figure 5) whereas hardly modified the number of DOE for the two other frequencies.

It has been shown repeatedly that the ultimate origin of harbor oscillations is the atmospheric forcing (Monserrat, et al., 1991; Monserrat, et al., 2006; Rabinovich, 2009). Both the AEMET and the GOFIMA records of atmospheric pressure have been used to characterize the prevailing meteorological conditions during the DOE, evaluating the low and high frequency behavior of the barometric field, respectively. The series corresponding to the oscillations of 16.5 min period has been in turn considered as representative of the Helmholtz mode of the harbor.

Although the occurrence of DOE coincides with low pressures, as shown in Figure 10 or 11, it is not a rule of thumb. Around 25% of cases are observed when the atmospheric pressure is above its mean, especially in winter months. The relevant point, however, is the notorious high frequency content in the atmospheric pressure records whenever short period oscillations are observed (see Figure 10, for example), a feature that is common to almost all the events identified. The high frequency contribution, however, is not completely resolved in the fifteen-minute-interval time series of GOFIMA, a fact that prevents the identification of the dominant frequency, if any. In any case, it is the advection of the disturbances by the atmospheric fronts that sweep the Iberian Peninsula from west to east that most likely triggers the harbor oscillations as they pass by.

With an amplitude of the atmospheric pressure disturbances typically O(1 hPa), the direct effect on the sea level would be oscillations of 1 cm amplitude under isostatic response, much

less than the observed ones. However, the high Q-value of the port of Málaga ensures an amplified response if the atmospheric pressure disturbances contain frequencies closer to the Helmholtz mode. The process of amplification consists of two steps, as it has been reported repeatedly in the literature (Rabinovich, 2009; Monserrat, et al., 2006). In a first step, atmospheric pressure disturbances transfer energy to the ocean at a much larger spatial scale than the harbor dimensions, for instance, by originating long ocean waves (Monserrat, et al., 1991). Lately, these waves excite the harbor modes acting at its open mouth.

Two kinds of atmosphere-sea coupling can be invoked for an efficient atmosphere-to-sea energy transfer: the Greenspan and the Proudman resonances. The Greenspan resonance (Greenspan, 1956) occurs when the along-shore component of the velocity of the atmospheric disturbances matches the phase speed of some of the natural modes of the edge waves. Let us carry out some computations for a specific situation: during the event showed in Figure 11, an atmospheric front was moving northeastward along the southern coast of the Iberian Peninsula. The displacement of a cloud mass in hourly EUMETSAT images (not shown) was used to make a guess of the speed of the front, which was estimated in $\sim$16 ms^{-1}, within the phase speed range of edge wave modes. Therefore, Greenspan resonance is a candidate mechanism for explaining this event (and others) of short period oscillations. Proudman resonance takes place when the phase speed of long oceanic waves equals the speed of the atmospheric pressure systems (Rabinovich, 2009). The phase speed of oceanic long waves, $c = \sqrt{gH}$, would match the progression speed of the front for H = 25m, a representative depth for the inner continental shelf. Proudman resonance is thus another very feasible possibility for efficient energy transfer. Whichever the case, the excitation of the harbor oscillations requires the arrival of waves at the harbor's mouth containing energy in the frequency band centered around 16.5^{-1} cpm that must have been previously transferred from the atmosphere by any of the mentioned mechanisms.

The effect of winds has also been addressed with inconclusive results. Although the events of short period oscillations are preferably observed under westerlies, it is also true that they occur with winds coming from other directions. The very large sampling interval of the available wind series (6 hours) is clearly inadequate for addressing the issue properly.

Acknowledgements

Model runs have been carried out in the supercomputer PICASSO by the Supercomputing and Bioinformatic Centre of the University of Málaga. Partial financial support was provided by the Regional Andalusian Government (RNM137). CC acknowledges the financial support within the action CTM2008-04150E.

References

Bentamy A. and Croize-Fillon D. Gridded surface wind fields from Metop/ASCAT measurements [Journal] // International Journal Of Remote Sensing. - 2012. - 6 : Vol. 33. - pp. 1729-1754.

Candela J. [et al.] The “Mad Sea” phenomenon in the Strait of Sicily [Journal] // J. Phys. Oceanogr.. - 1999. - Vol. 29. - pp. 2210-2231.

Delgado J. [et al.] Short period sea level oscillations at Strait of Gibraltar: Observations versus model results [Journal] // Estuarine, Coastal and Shelf Science. - 2011. - 2-3 : Vol. 95. - pp. 307-313.

Djumagaliev V. A., Rabinovich A. B. and Fine I. V. Theoretical and experimental estimation of transfer peculiarities of the Malokurilsk Bay coast, the Island of Shikotan [Journal] // Atmosph. Oceanic Phys.. - 1994. - Vol. 30. - pp. 680-686.

Drago A. Numerical modelling of coastal seiches in Malta [Journal] // Physics and Chemistry of the Earth. - 2008. - 3-4 : Vol. 33. - pp. 260-275.

Emery W. J. and E. Thomson R. Time-series Analysis Methods [Book Section] // Data Analysis Methods in Physical Oceanography. - Amsterdam : Elsevier Science, 2001.

Garcies M., Gomis D. and Monserrat S. Pressure-forced seiches of large amplitude in inlets of the Balearic Islands. Part II: Observational study [Journal] // J. Phys. Oceanogr.. - 1996. - Vol. 101. - pp. 6453-6467.

Gill E. Atmosphere-Oceans Dynamics [Book]. - London : Academic Press, Inc., 1982. - International Geophysics Series : Vol. 30 : p. 662.

Gomis D., Monserrat S. and Tintoré J. Pressure-forced seiches of large amplitude in [Journal] // J. Geophys. Res.. - 1993. - Vol. 98. - pp. 14437-14445.

Greenspan H. P. The generation of edge waves by moving pressure disturbances [Journal] // J. Fluid Mech.. - 1956. - Vol. 1. - pp. 574-592.

Hibiya T. and Kajiura K. Origin of ‘Abiki’ phenomenon (kind of seiches) in Nagasaki Bay [Journal] // J. Oceanogr. Soc. Japan. - 1982. - Vol. 38. - pp. 172-182.

Marshall J. [et al.] A finite-volume, incompressible Navier Stokes model for studies of the ocean on parallel computers [Journal] // J. Geophys. Res.. - 1997. - Vol. 102(C3). - pp. 5753-5766.

Marshall J. [et al.] Hydrostatic, quasi-hydrostatic, and nonhydrostatic ocean modeling [Journal] // J. Geophys. Res.. - 1997. - Vol. 102(C3). - pp. 5733-5752.

Monserrat S. and Thorpe A. J. Gravity-wave observations usoing an array of microbarograhs in the Balearic Islands [Journal] // Q. J. Roy. Meteor. Soc.. - 1992. - Vol. 118. - pp. 259-282.

Monserrat S., Ibbetson A. and Thorpe A. J. Atmospheric gravity waves and the 'rissaga' phenomenon [Journal] // Q. J. Roy. Meteor. Soc.. - 1991. - Vol. 117. - pp. 553-570.

Monserrat S., Vilibic I. and Rabinovich A. B. Meteotsunamis: atmospherically induced destructive ocean waves in the tsunami frequency band [Journal] // Nat. Hazards Earth Syst. Sci.. - 2006. - Vol. 6. - pp. 1035-1051.

Muñoz M. V. Análisis de las direcciones de los vientos en Andalucía [Journal] // Nimbus. - 1998. - Vol. 1. - pp. 153-168.

Oppenheim A. V. and Schafer R. W. Discrete-time Signal Processing [Book]. - [s.l.] : Prentice Hall, 1999. - p. 879.

Pawlowicz R., Beardsley B. and Lentz S. Classical tidal harmonic analysis including error estimates in MATLAB using T_TIDE [Journal] // Computers and Geosciences. - 2002. - Vol. 28. - pp. 929-937.

Rabinovich A. B., Monserrat S. and Fine I. V. Numerical modeling of extreme seiche oscillations in the region of Balearic Islands [Journal] // Oceanology. - 1999. - Vol. 39. - pp. 16-24.

Rabinovich Alexander B. Seiches and Harbor Oscillations [Book Section] // Handbook of Coastal and Ocean Engineering / book auth. Kim Y. C.. - Singapoure : World Scientific Publ., 2009.

Rueda F. and Schladow S. Quantitative Comparison of Models for Barotropic Response of Homogeneous Basins [Journal] // Journal of Hydraulic Engineering. - 2002. - 2 : Vol. 128. - pp. 201-213.

Sawaragi T. and Kubo M. The motions of a moored ship in a harbor basin [Conference] // Proc. of 18th Int. Conf. on Coastal, ASCE. - 1982. - pp. 2743-2762.

Wilson B. W. Seiches [Book Section] // Advances in Hydroscience / book auth. Chow Ven Te. - New York : Academic Press, 1972.

A. Appendix: resonant oscillations from a barotropic model

The procedure to derive the structure and natural frequencies of resonant oscillations in the harbor from a barotropic model simulation is described. The source code of the Massachusetts Institute of Technology General Circulation Model (MITgcm) is used to conduct our experiments. We are interested in long surface gravity waves, thus a free-surface, barotropic, and hydrostatic configuration of the model is applied. Additionally, the waves in question are linear (small-amplitude) and basically unaffected by the Earth's rotation (of much larger frequency than the inertial frequency), and therefore both the advective and the Coriolis terms are removed from the momentum equation. The model is initialized with sea water of constant density, and time-stepping for the tracer equations is also disabled in order to prevent unnecessary calculations. With this configuration the equations solved are the so-called shallow-water or barotropic long-wave equations.

The model domain has an area of 6x6 km^2 and has been discretized with a regular grid of x=y=10 m resolution. In the vertical there is only one vertical level of variable thickness that fits the local bottom depth (partial-step representation of the bottom topography). At the solid boundaries no-slip boundary conditions are set. Additionally, explicit horizontal viscosity is included, $\nu_H=1x10^{-3}m^2s^{-1}$, and a quadratic bottom drag $\tau=C_d\rho u^2$ has been imposed at the bottom boundary, with a drag coefficient $C_d=2x10^{-3}$. This enables some energy dissipation in our model. The time step is set to $\Delta t=0.1s$, which satisfies the CFL stability condition for surface gravity waves.

The model is forced by prescribing the velocity field:

$$u = 0, \qquad v = U\sin(2\pi f t);$$

$$u = -U\sin(2\pi f t), \qquad v = 0;$$

at the southern and eastern open lateral boundaries, respectively. This produces an overall sea level oscillation of frequency f and amplitude

$$SSH_A = \frac{A_{lb}U}{2\pi f A_s}$$

where A_{lb} denotes the total area of the lateral boundaries (south plus east), and A_s is the area of the sea surface. In the following, for a given frequency $f = f_r$, U is set so that SSH_A=1.5 cm. This mimics the effect of remote atmospheric pressure perturbations of 1.5 hPa amplitude oscillating at the given frequency.

The experiment lasts for 8 hours and the model outputs are written every minute. Consider, for instance the run corresponding to f_r=30^{-1}min^{-1}. From the model outputs the resonant frequencies (f_0 and f_1) can be identified from the maxima of a SSH spectra, much like in Figure A1.

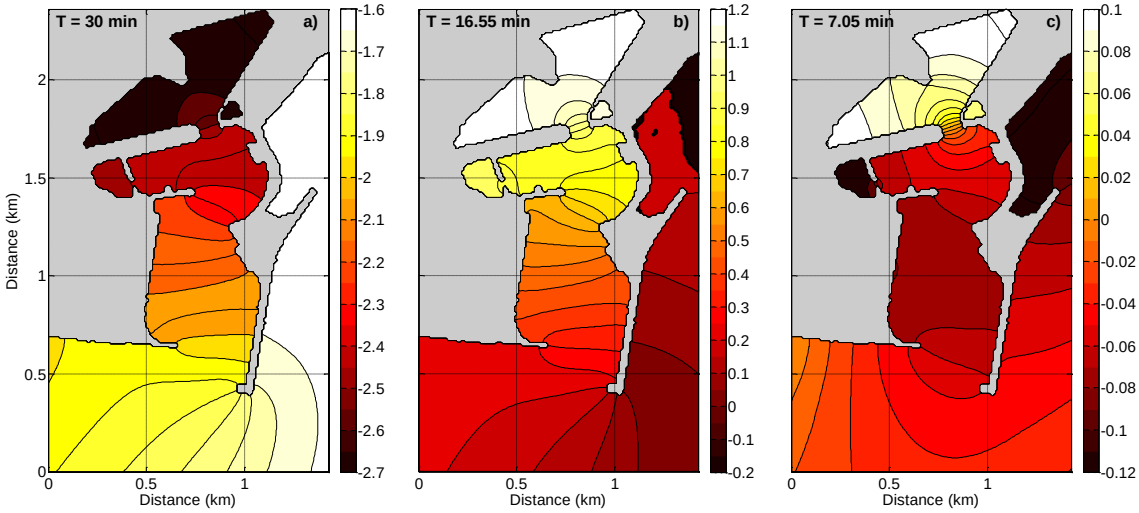

Figure A1 - Panels a) A_r, b) A_0 and c) A_1 for the run with forcing frequency f_r = 30^{-1} cpm. Sea level amplitude is in cm. The amplitude sign is assigned depending upon the value of the corresponding phase, positive and negative for ϕ_k = 0 and ϕ_k = π ($k = r,\ 0,\ 1$), respectively.

To explore the spatial structure of SSH amplitudes at the frequencies of interest, the sea surface is expressed as:

$$SSH(x,y,t) = \overline{SSH}(x,y) + \sum_{k=r,0,1} A_k(x,y)\cos[2\pi f_k t + \phi_k(x,y)] + res$$

Here the bar denotes time-average and res is a (small) residue. SSH amplitude and phase, A_k and ϕ_k, are obtained from the Fourier transform of the series. Figure A1 shows A_k (k = r, 0, 1), whose sign in every grid point has been assigned depending upon the value of the associated phase ϕ_k; positive and negative for ϕ_k=0 and ϕ_k=π, respectively. These are the only values that phases take in the harbor and its surroundings.

A_0 maintains sign within the harbor, which means that the SSH oscillate in-phase. Amplitudes amplify towards the head of the harbor, and presents a nodal line lying some hundred meters away from its entrance. A_1 also presents a nodal line outside the harbor, and a second one at the narrowest harbor passage. We can therefore state that A_0 and A_1 are the n=0 (Helmholtz), and n=1 resonant modes of the harbor, respectively.

Additionally, the amplification factor of the frequency f_r can be calculated from A_r. SSH oscillations have 1.5 cm amplitude outside the harbor, and the mean value of A_r within it is ~2.2 cm, which implies a mean amplification factor of 1.46. It is important to note that the amplification factors derived here must be definitely sensitive to model parameters involving friction (bottom drag, side drag, and eddy viscosity coefficients). To this end, further runs, with different values of the drag coefficient, have been carried and results are fully satisfying. However, some further tests may be desirable in the future to completely assess the sensitivity of the model for the amplification response.

Fig 1

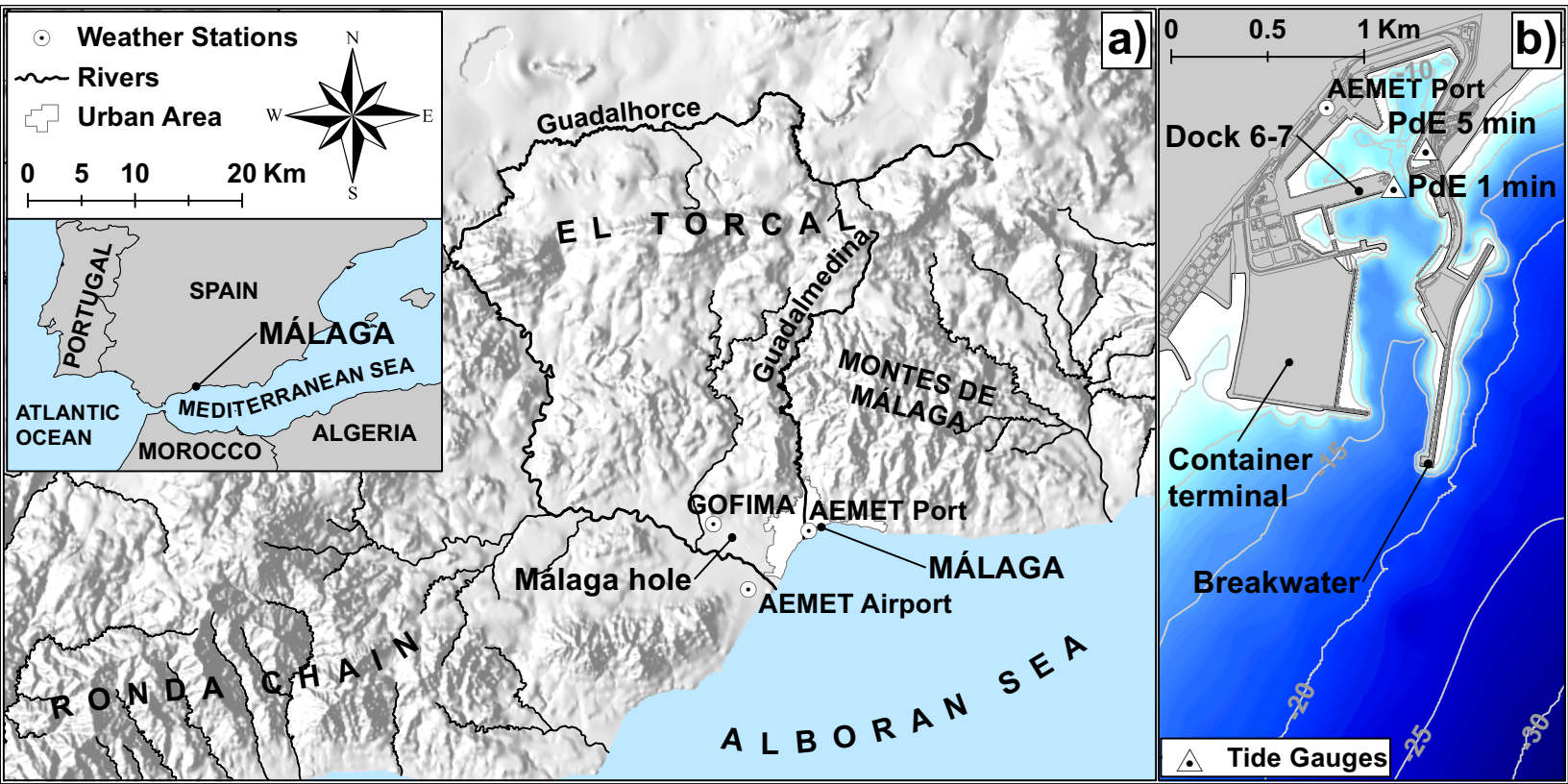
Weather Stations
Rivers
Urban Area
0 5 10 20 Km
N
W
E
S
PORTUGAL
SPAIN
MÁLAGA
MEDITERRANEAN SEA
ATLANTIC OCEAN
MOROCCO
ALGERIA
a)
Guadalhorce
EL TORCAL
Guadalmedina
MONTES DE MÁLAGA
GOFIMA
AEMET Port
MÁLAGA
Málaga hole
AEMET Airport
RONDA CHAIN
ALBORAN SEA
b)
0 0.5 1 Km
AEMET Port
PdE 5 min
Dock 6-7
PdE 1 min
Container terminal
Breakwater
Tide Gauges

Fig 2a

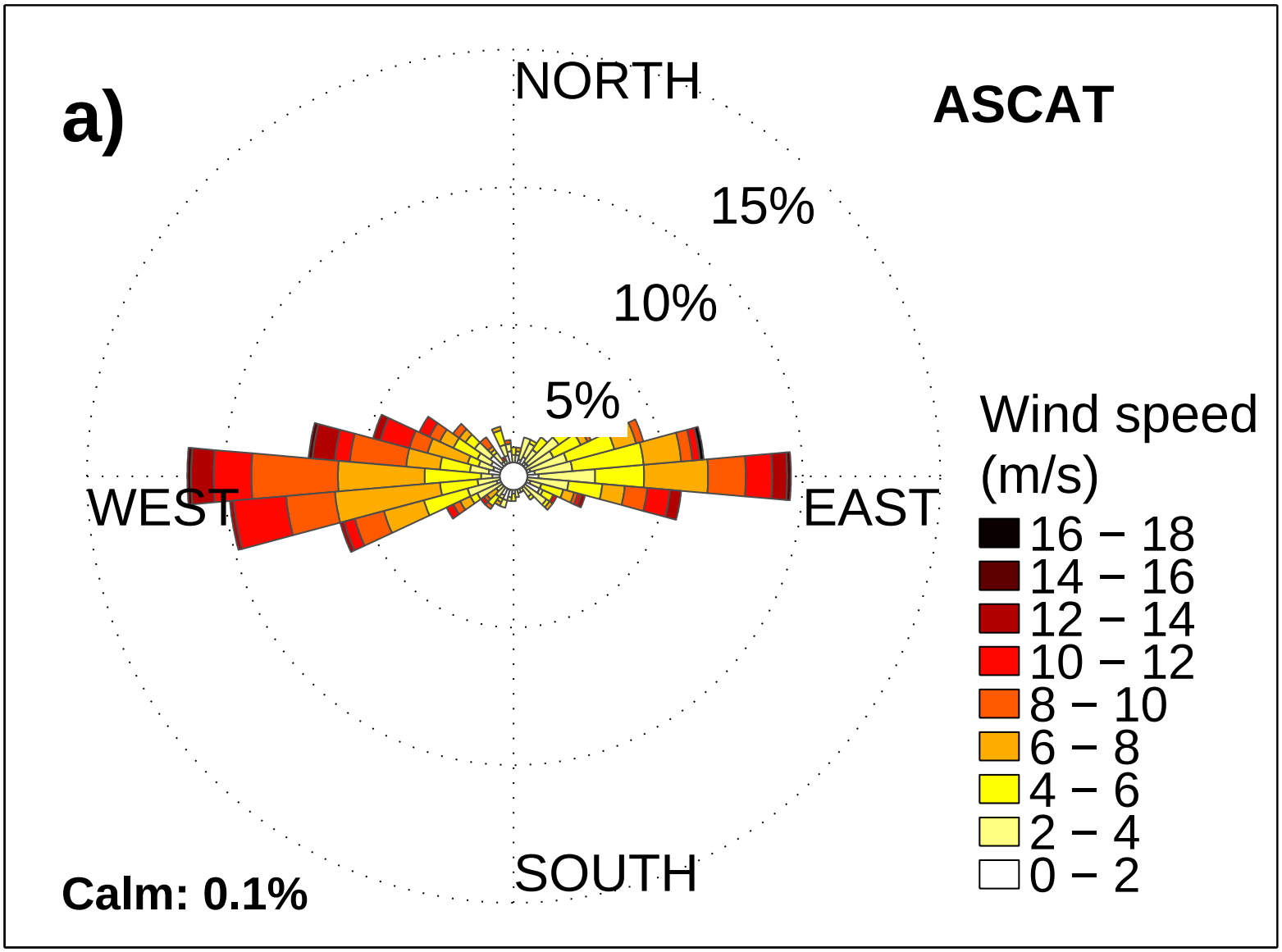
a)
NORTH
ASCAT
15%
10%
5%
WEST
EAST
SOUTH
Wind speed
(m/s)
16 – 18
14 – 16
12 – 14
10 – 12
8 – 10
6 – 8
4 – 6
2 – 4
0 – 2
Calm: 0.1%

Fig 2b

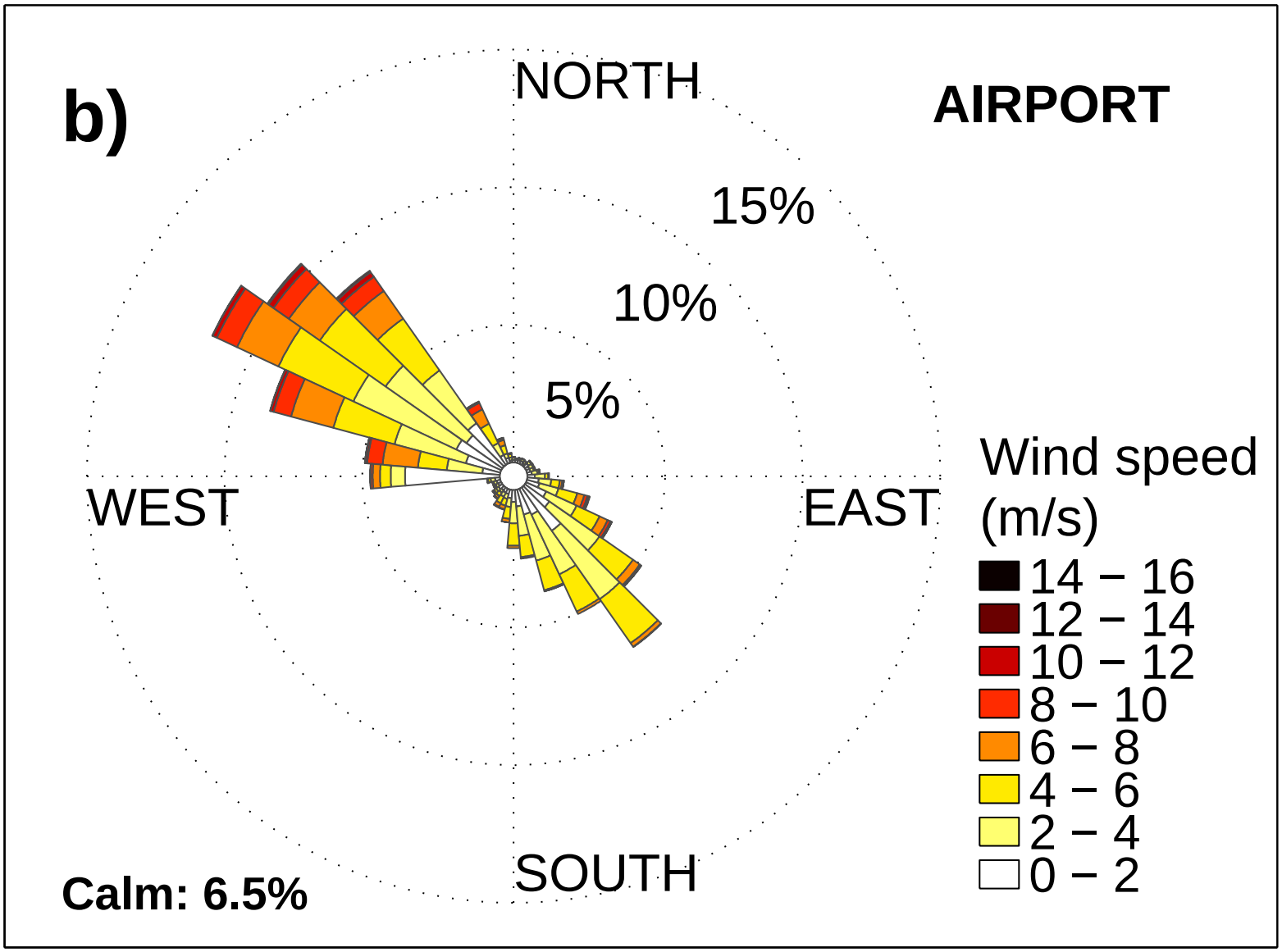
b)
NORTH
AIRPORT
15%
10%
5%
WEST
EAST
SOUTH
Wind speed
(m/s)
14 – 16
12 – 14
10 – 12
8 – 10
6 – 8
4 – 6
2 – 4
0 – 2
Calm: 6.5%

Fig 2c

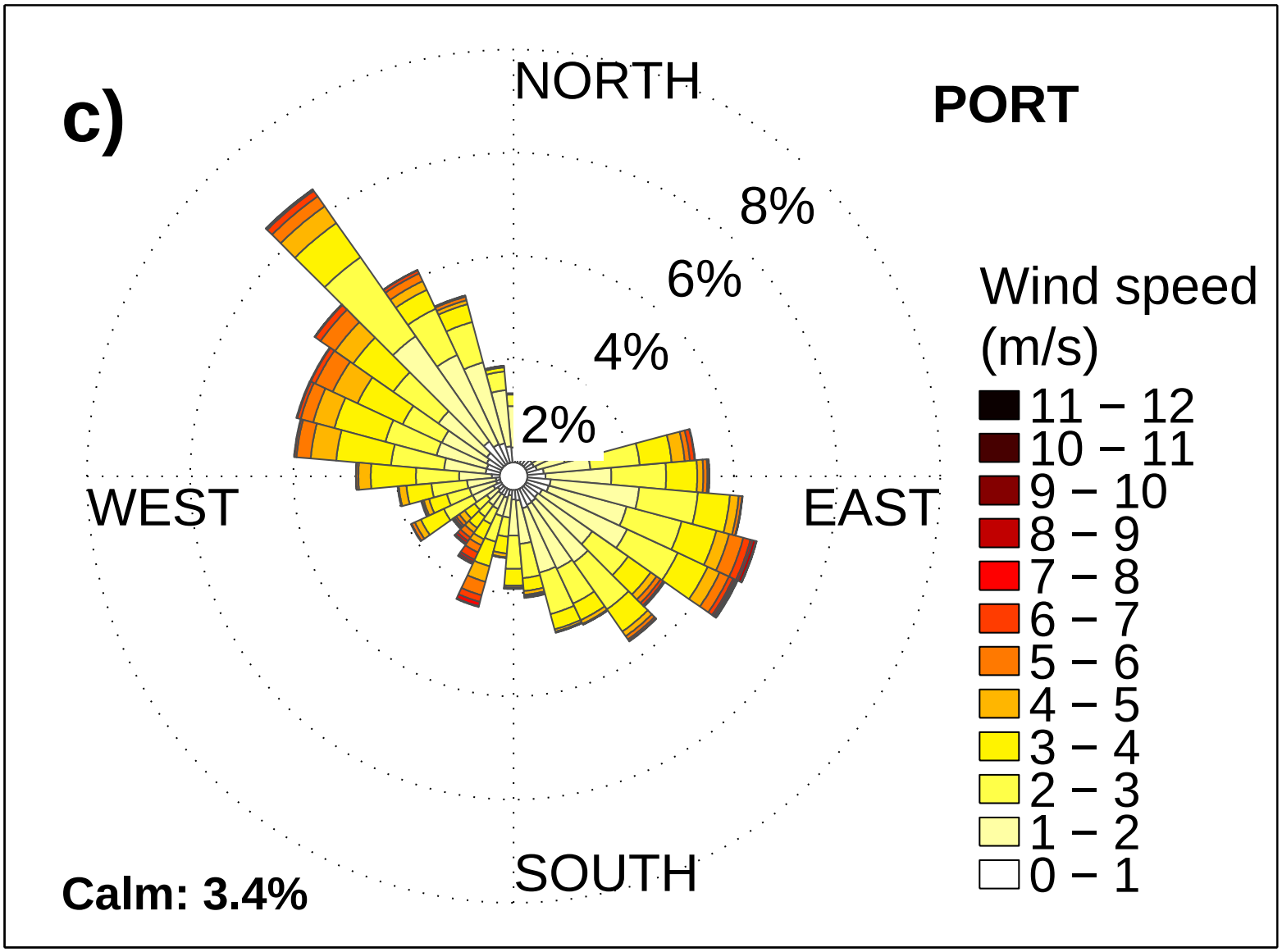
c)
PORT
NORTH
8%
6%
4%
2%
WEST
EAST
SOUTH
Calm: 3.4%
Wind speed (m/s)
11 – 12
10 – 11
9 – 10
8 – 9
7 – 8
6 – 7
5 – 6
4 – 5
3 – 4
2 – 3
1 – 2
0 – 1

Fig 3

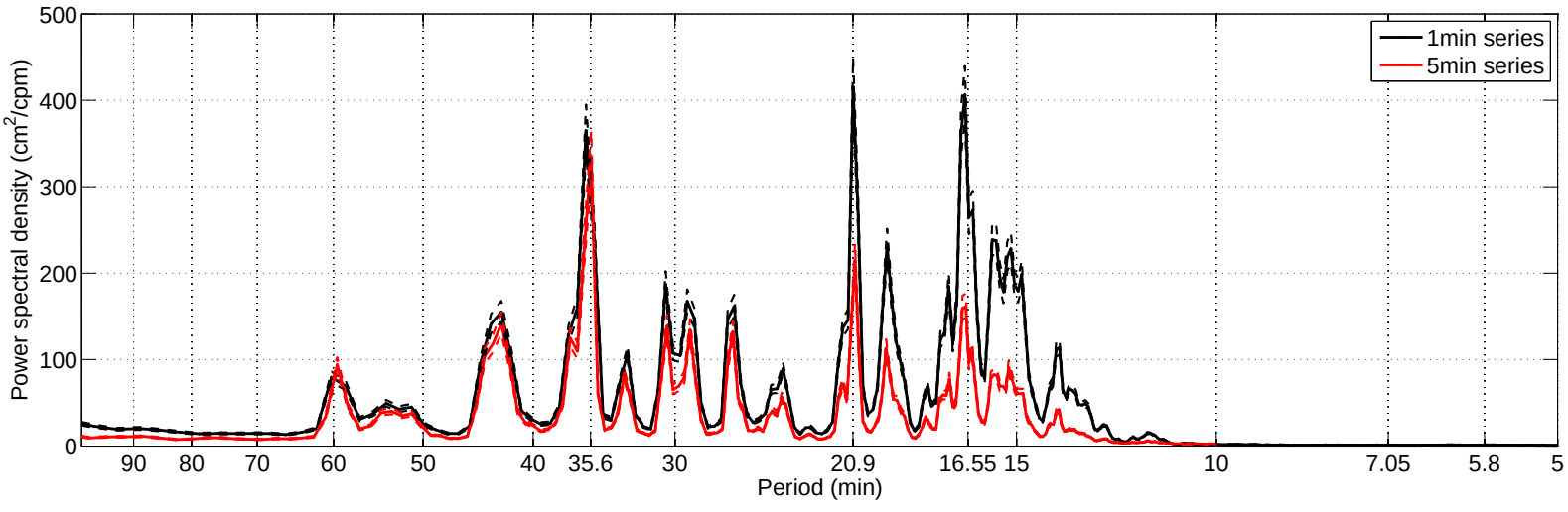
1min series
5min series
Power spectral density (cm²/cpm)
Period (min)
500
400
300
200
100
0
90
80
70
60
50
40
35.6
30
20.9
16.55
15
10
7.05
5.8
5

Fig 4a

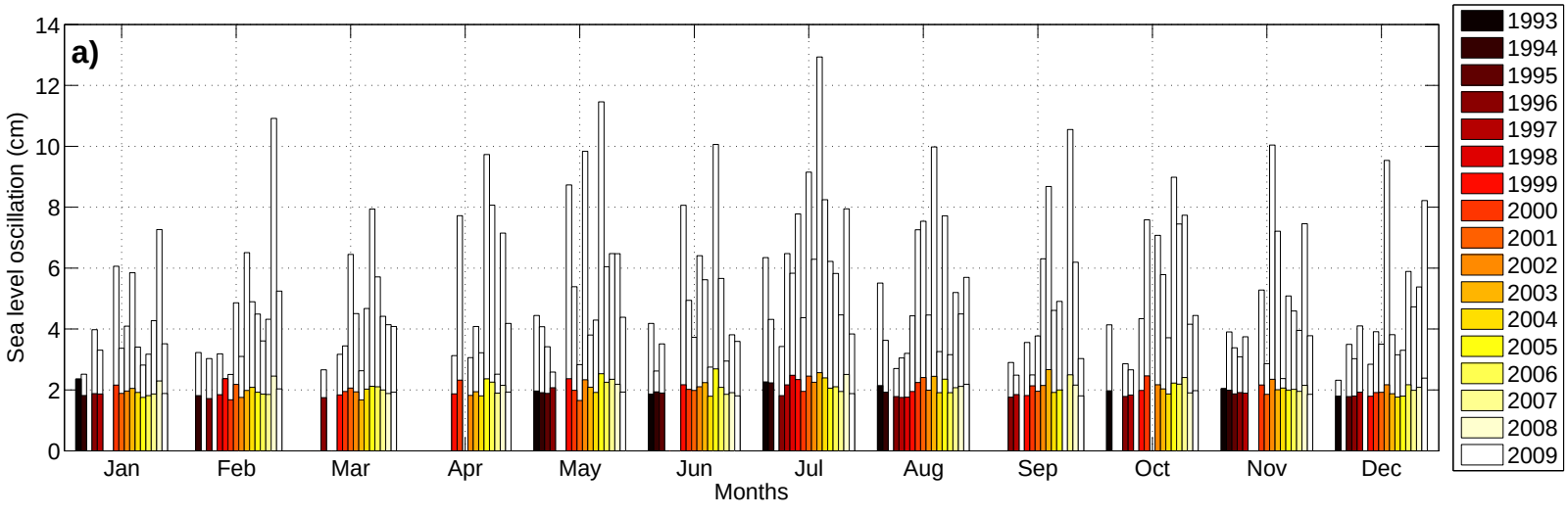
a)
Sea level oscillation (cm)
0
2
4
6
8
10
12
14
Jan
Feb
Mar
Apr
May
Jun
Jul
Aug
Sep
Oct
Nov
Dec
Months
1993
1994
1995
1996
1997
1998
1999
2000
2001
2002
2003
2004
2005
2006
2007
2008
2009

Fig 4b

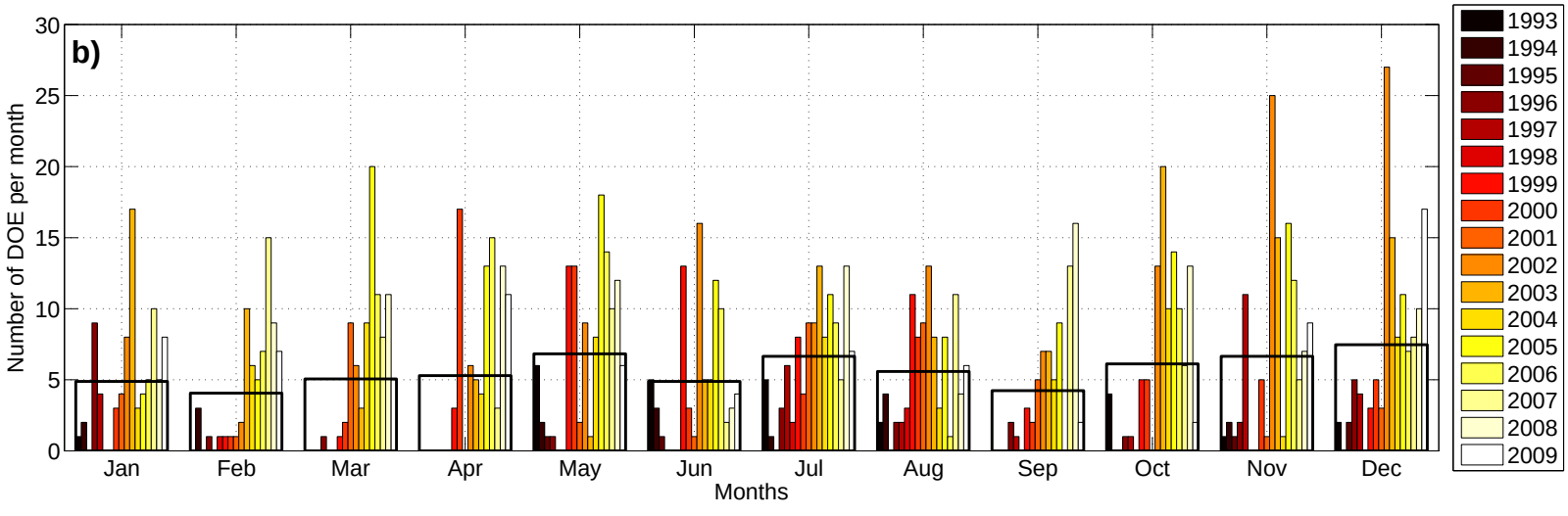
b)
Number of DOE per month
Months
Jan
Feb
Mar
Apr
May
Jun
Jul
Aug
Sep
Oct
Nov
Dec
0
5
10
15
20
25
30
1993
1994
1995
1996
1997
1998
1999
2000
2001
2002
2003
2004
2005
2006
2007
2008
2009

Fig 5

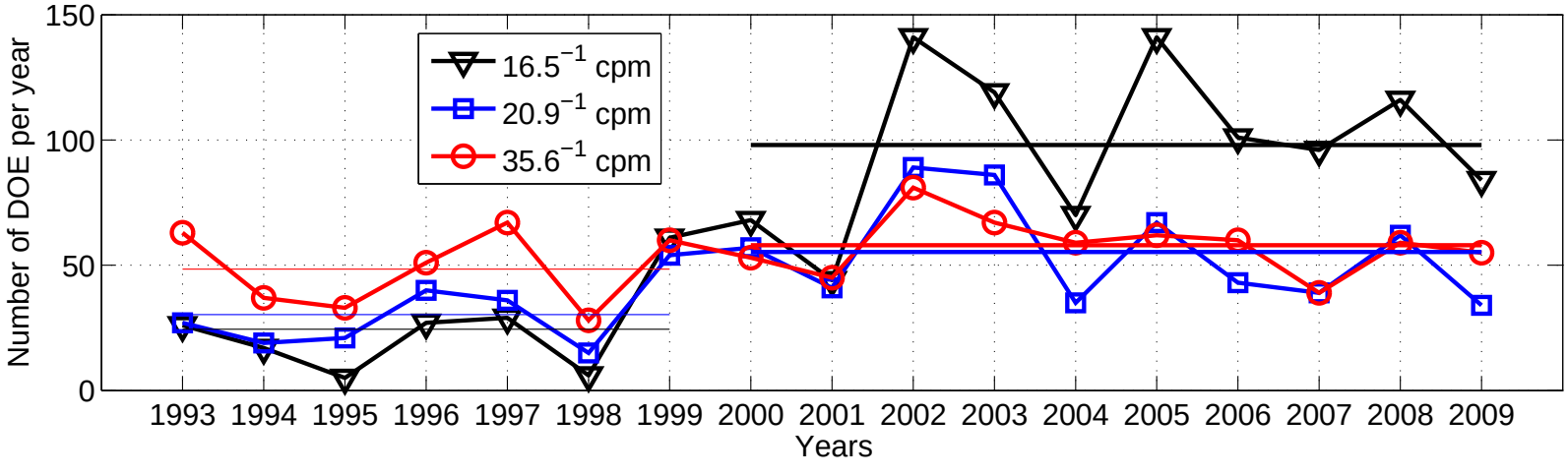
150
100
50
0
Number of DOE per year
16.5^{-1} cpm
20.9^{-1} cpm
35.6^{-1} cpm
1993 1994 1995 1996 1997 1998 1999 2000 2001 2002 2003 2004 2005 2006 2007 2008 2009
Years

Fig 6a

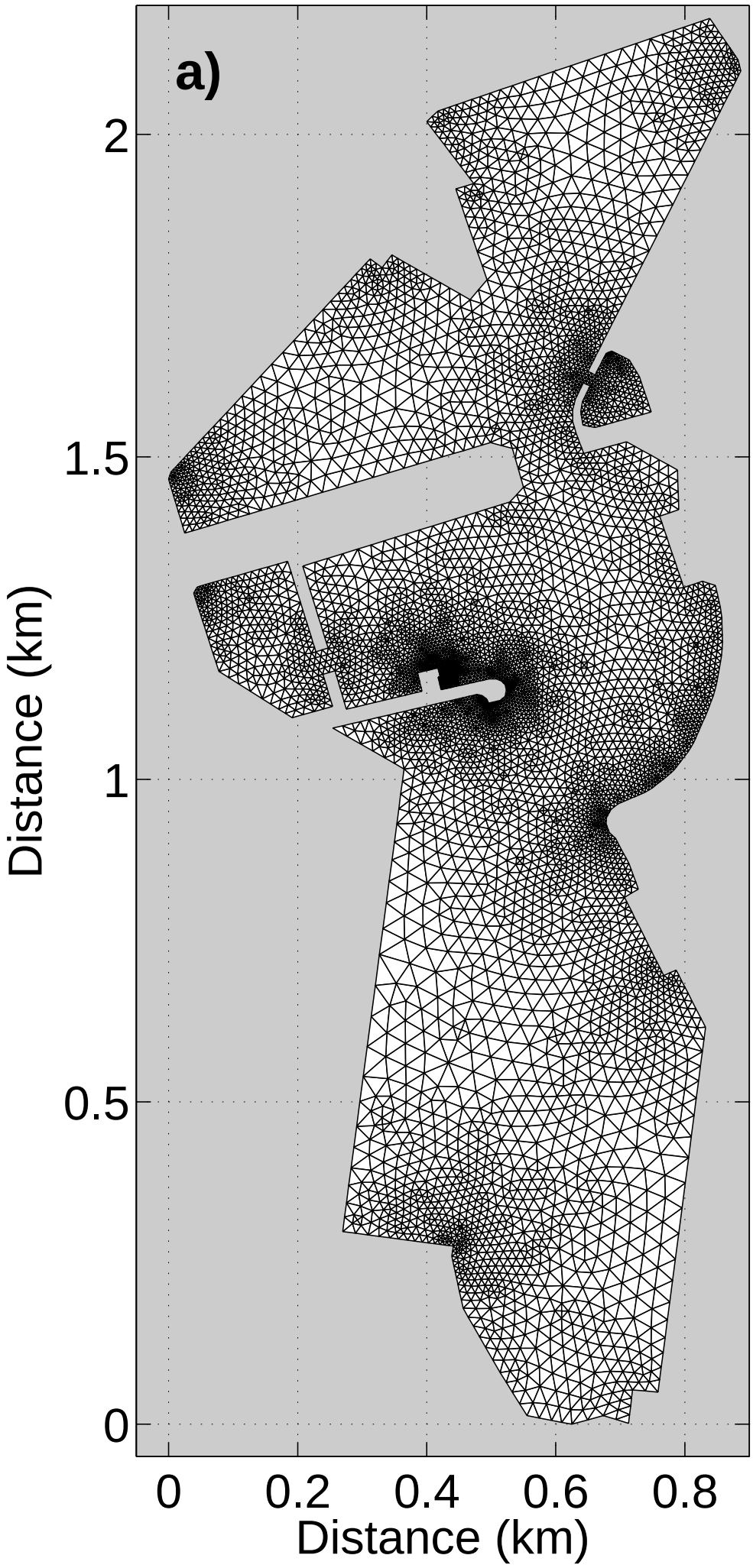

Fig 6b

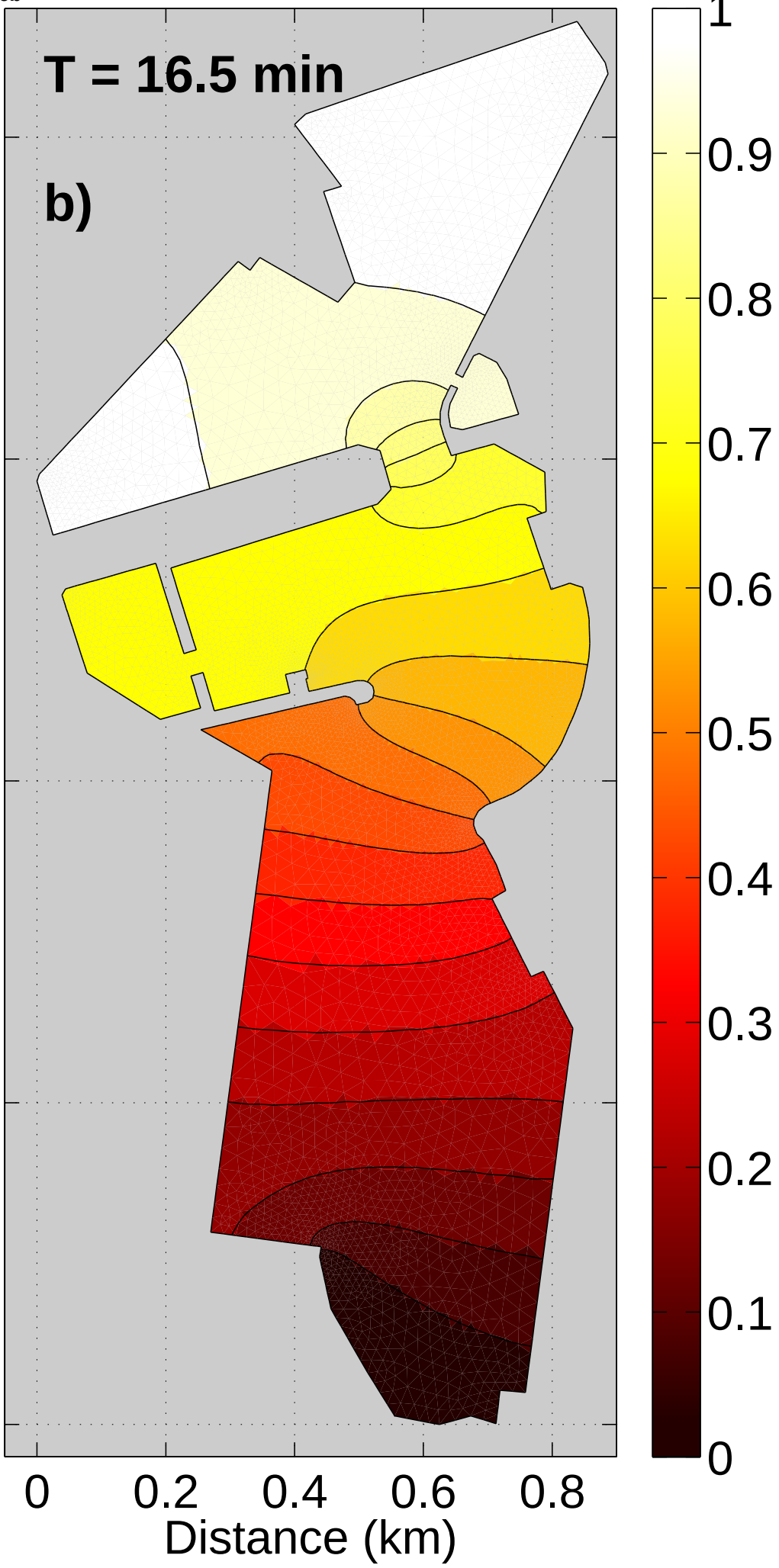

Fig 6c

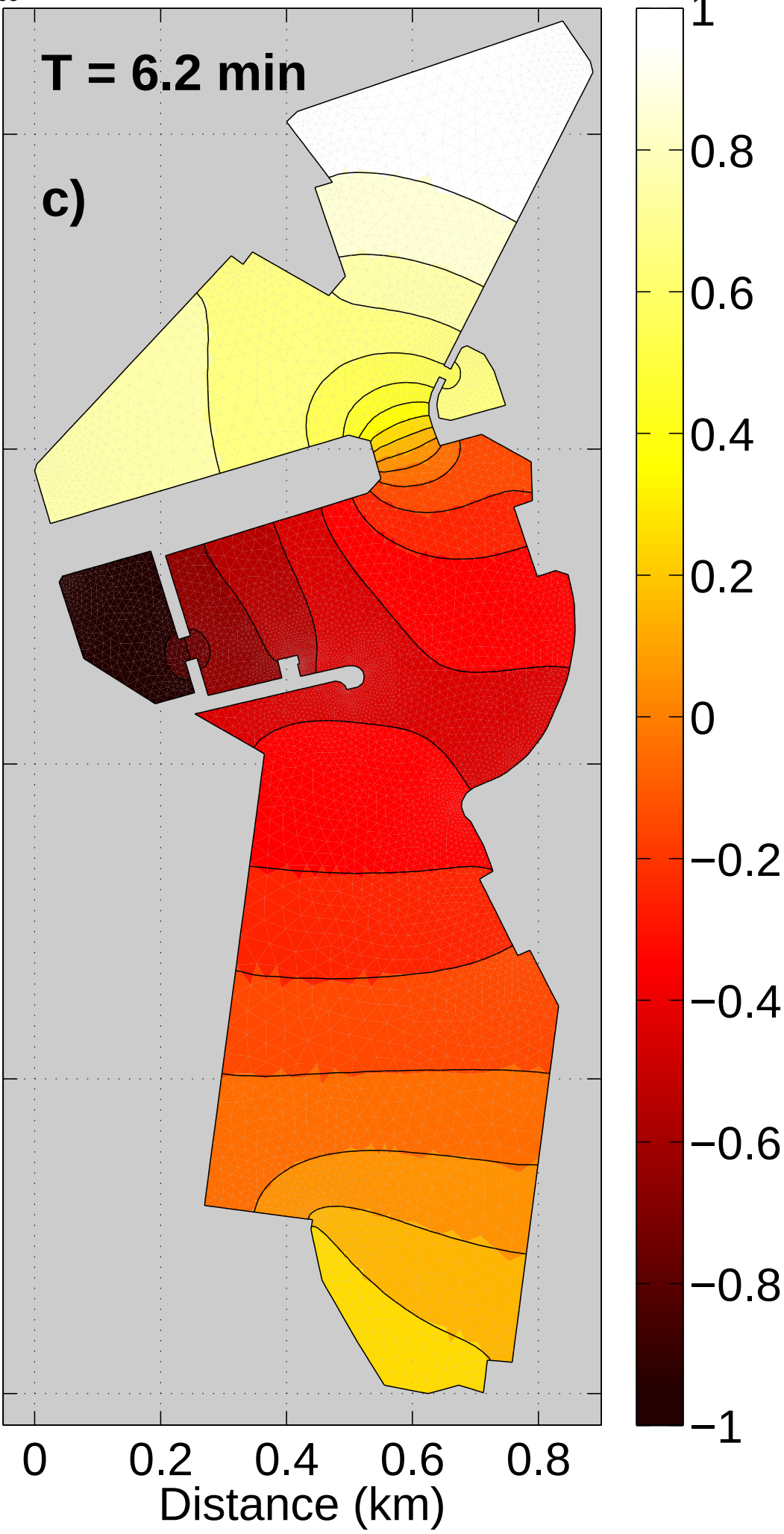

Fig 7a

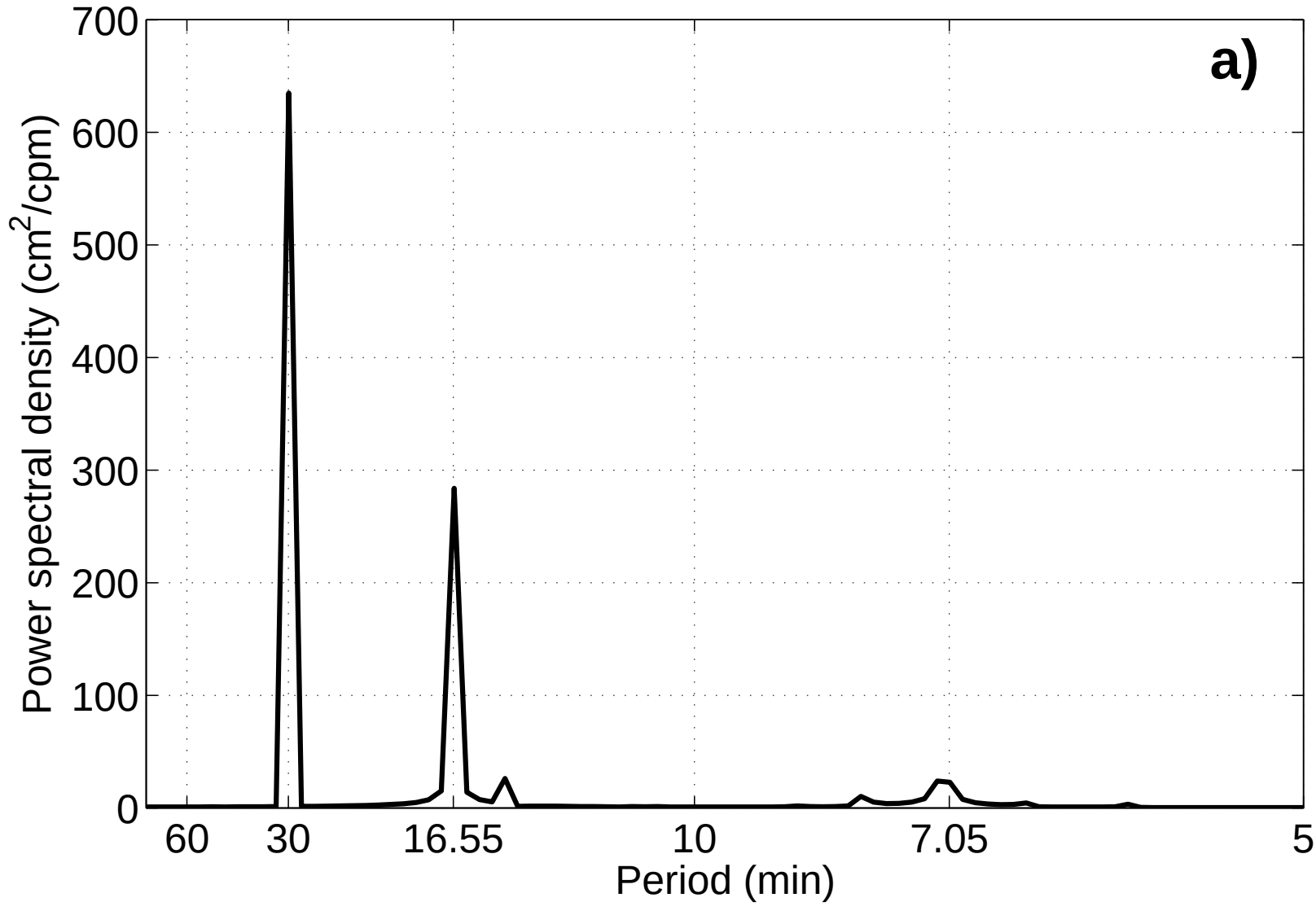
a)
Power spectral density (cm^2/cpm)
700
600
500
400
300
200
100
0
60
30
16.55
10
7.05
5
Period (min)

Fig 7b

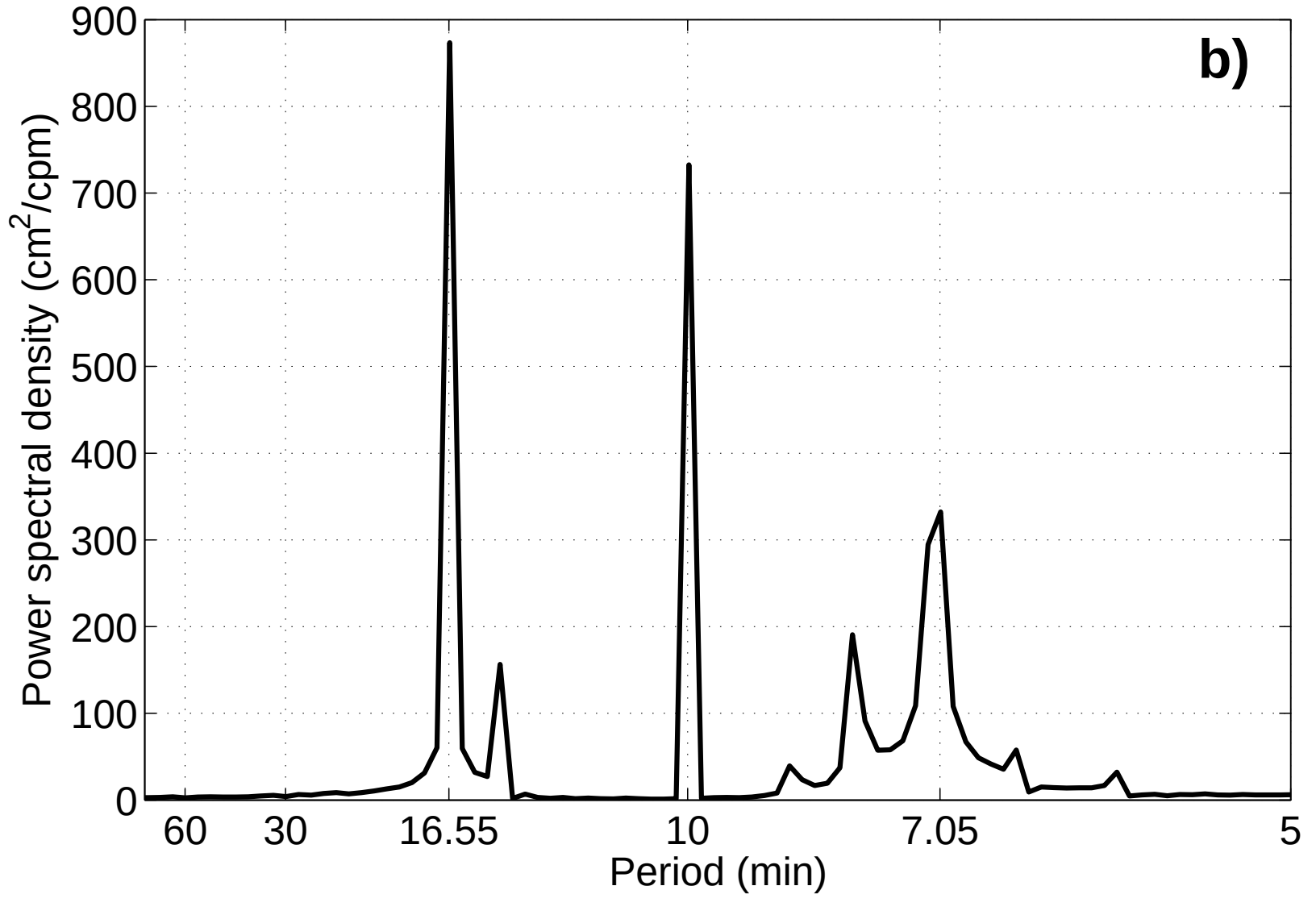
b)
Power spectral density (cm^2/cpm)
900
800
700
600
500
400
300
200
100
0
60
30
16.55
10
7.05
5
Period (min)

Fig 8

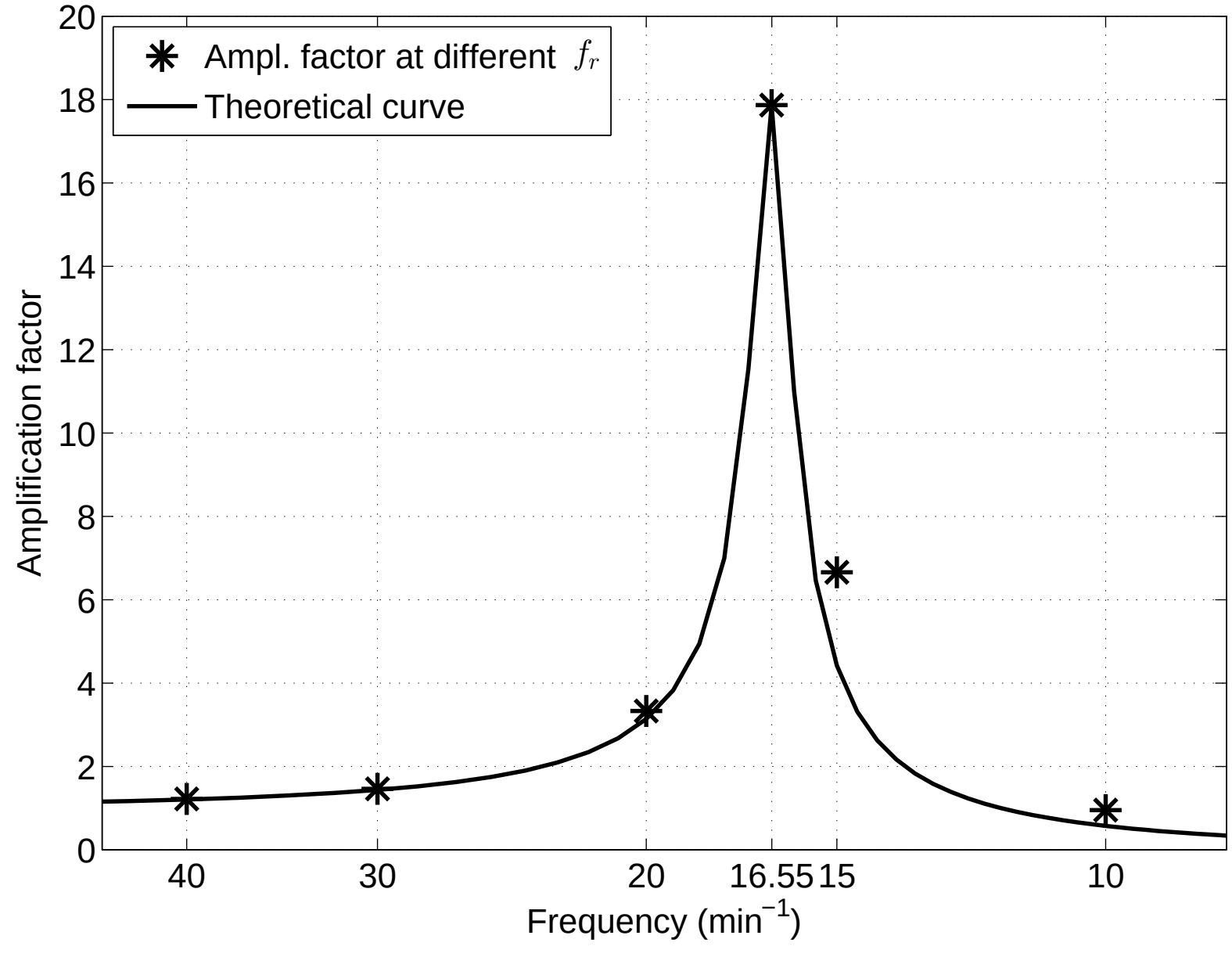
Ampl. factor at different f_r
Theoretical curve
Amplification factor
Frequency (min^{-1})
0
2
4
6
8
10
12
14
16
18
20
40
30
20
16.55
15
10

Fig 9

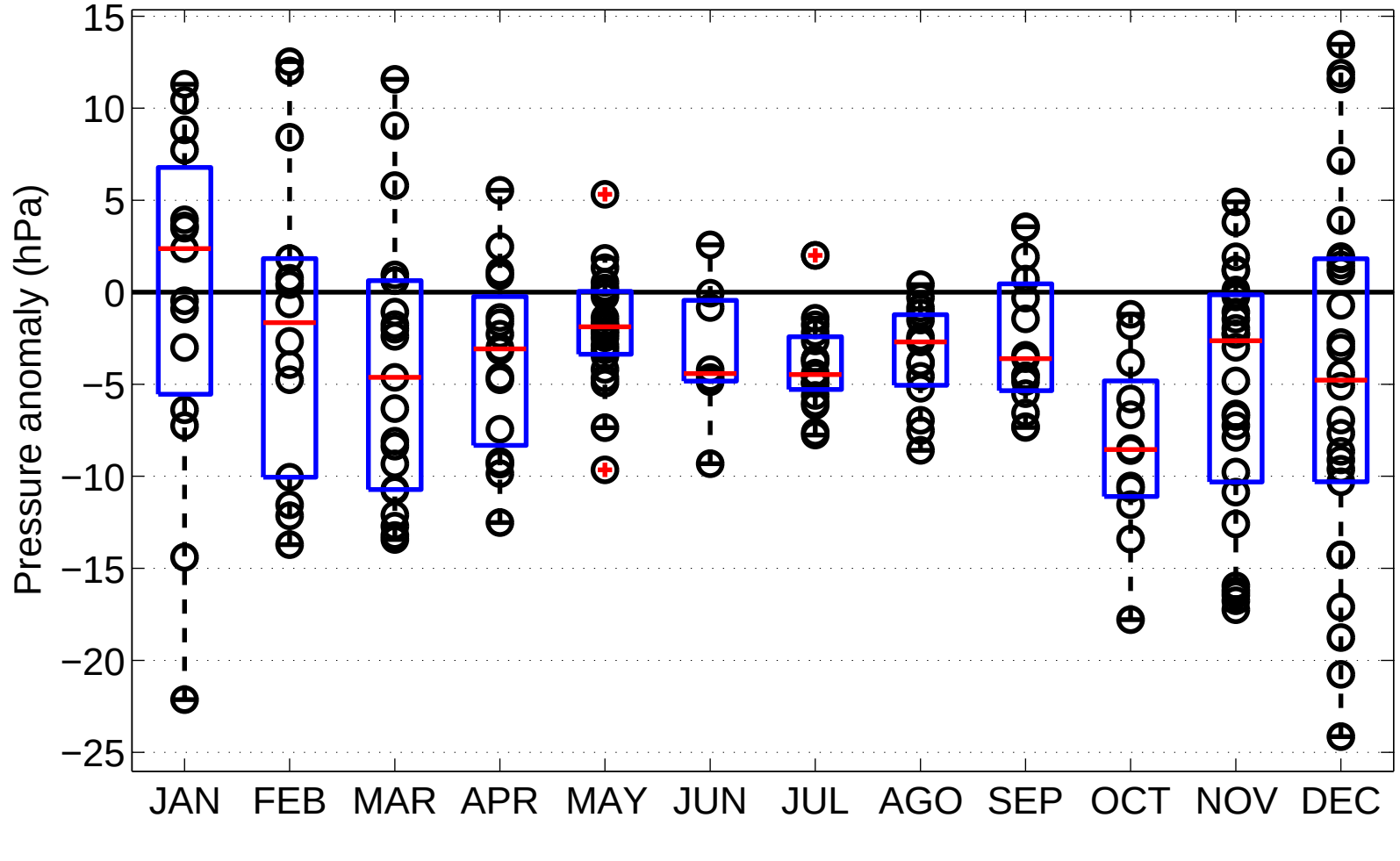
Pressure anomaly (hPa)
15
10
5
0
−5
−10
−15
−20
−25
JAN
FEB
MAR
APR
MAY
JUN
JUL
AGO
SEP
OCT
NOV
DEC

Fig 10

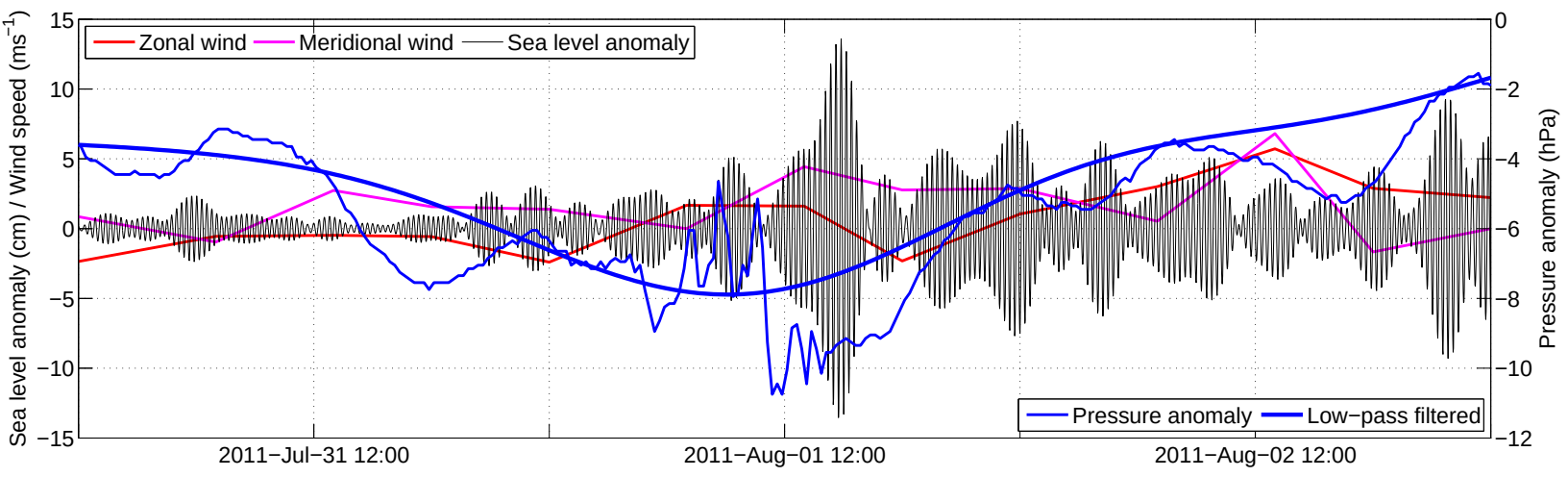
Zonal wind
Meridional wind
Sea level anomaly
Pressure anomaly
Low−pass filtered
Sea level anomaly (cm) / Wind speed (ms^{-1})
Pressure anomaly (hPa)
15
10
5
0
−5
−10
−15
0
−2
−4
−6
−8
−10
−12
2011−Jul−31 12:00
2011−Aug−01 12:00
2011−Aug−02 12:00

Fig 11

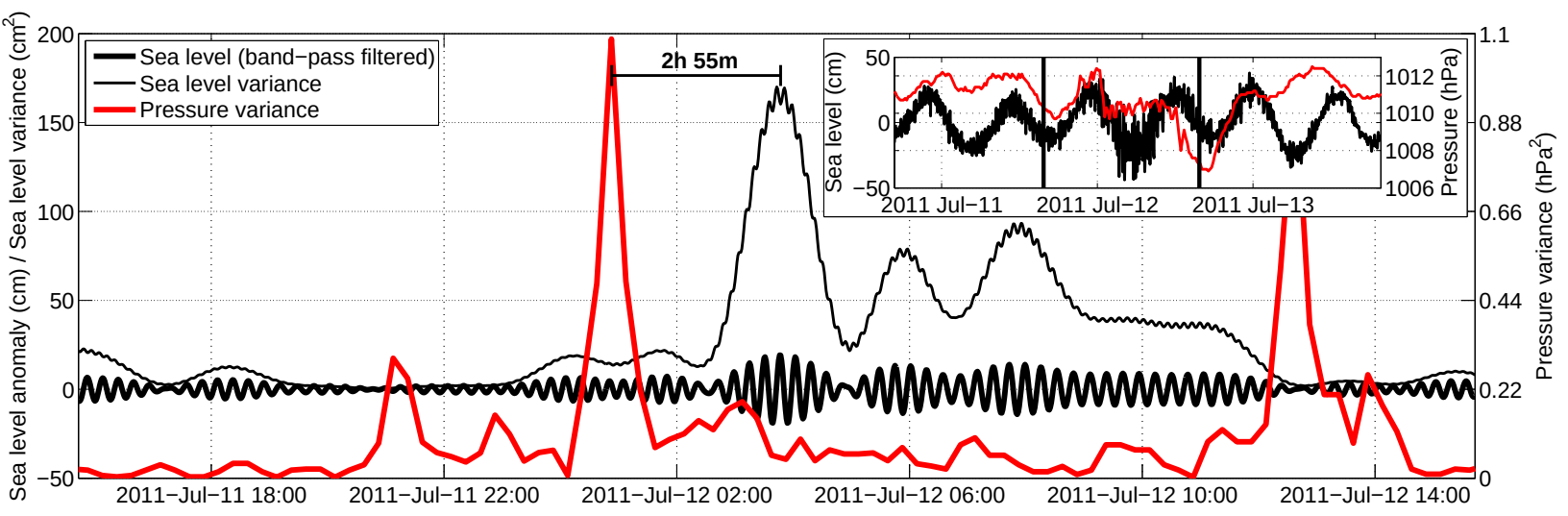
Sea level (band−pass filtered)
Sea level variance
Pressure variance
2h 55m
Sea level anomaly (cm) / Sea level variance (cm^2)
Pressure variance (hPa^2)
200
150
100
50
0
−50
1.1
0.88
0.66
0.44
0.22
0
2011−Jul−11 18:00
2011−Jul−11 22:00
2011−Jul−12 02:00
2011−Jul−12 06:00
2011−Jul−12 10:00
2011−Jul−12 14:00
Sea level (cm)
Pressure (hPa)
50
0
−50
1012
1010
1008
1006
2011 Jul−11
2011 Jul−12
2011 Jul−13

Fig A1a

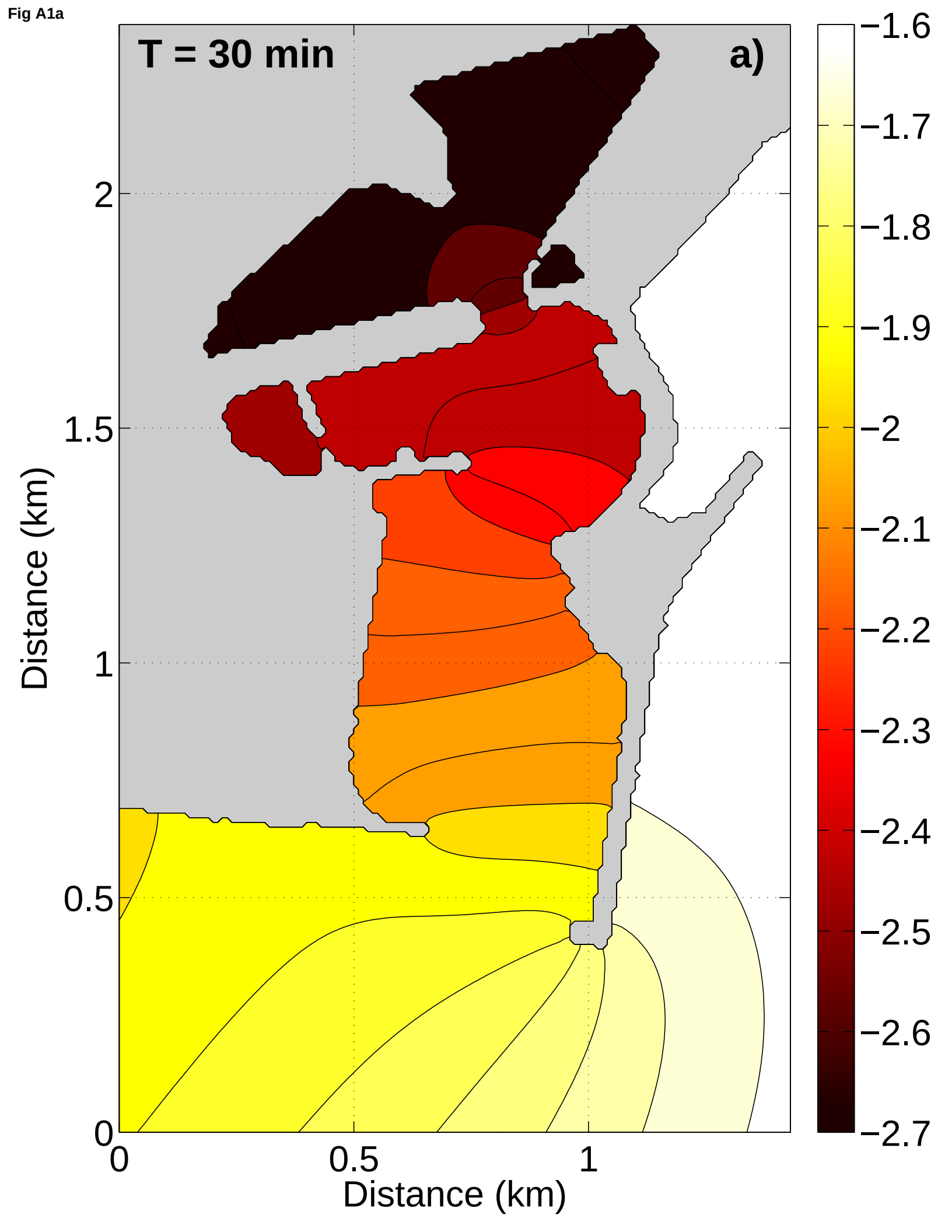
T = 30 min
a)
Distance (km)
Distance (km)
0
0.5
1
1.5
2
−1.6
−1.7
−1.8
−1.9
−2
−2.1
−2.2
−2.3
−2.4
−2.5
−2.6
−2.7

Fig A1b

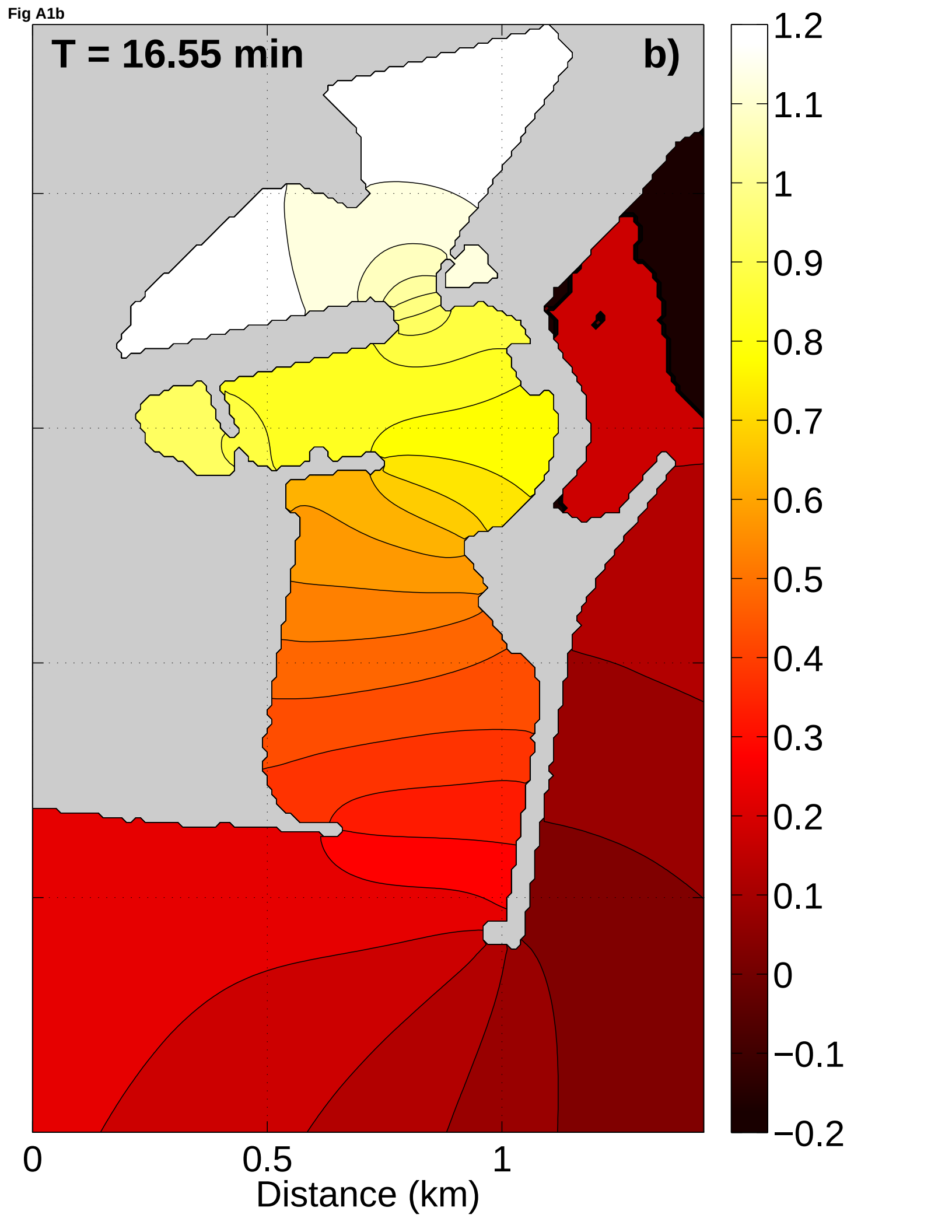
T = 16.55 min
b)
1.2
1.1
1
0.9
0.8
0.7
0.6
0.5
0.4
0.3
0.2
0.1
0
−0.1
−0.2
0
0.5
1
Distance (km)

Fig A1c

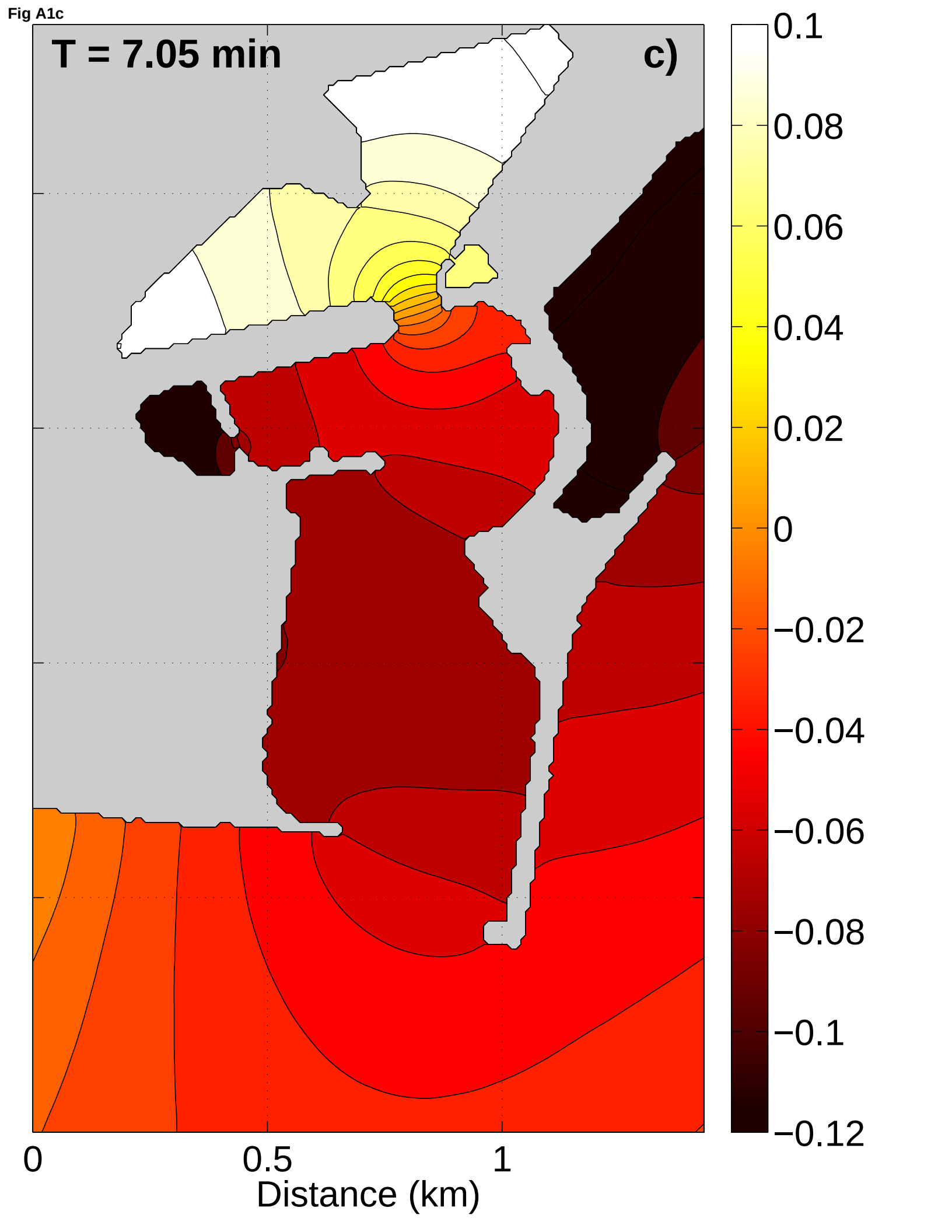
T = 7.05 min
c)
0.1
0.08
0.06
0.04
0.02
0
−0.02
−0.04
−0.06
−0.08
−0.1
−0.12
0
0.5
1
Distance (km)